The Astrophysical Journal, 746:85 (24pp), 2012 February 10 doi:10.1088/0004-637X/746/1/85

THE *HUBBLE SPACE TELESCOPE* CLUSTER SUPERNOVA SURVEY. V. IMPROVING THE DARK-ENERGY CONSTRAINTS ABOVE $z > 1$ AND BUILDING AN EARLY-TYPE-HOSTED SUPERNOVA SAMPLE*

N. Suzuki[1,2], D. Rubin[1,2], C. Lidman[3], G. Aldering[1], R. Amanullah[2,4], K. Barbary[1,2], L. F. Barrientos[5], J. Botyanszki[2], M. Brodwin[6,41], N. Connolly[7], K. S. Dawson[8], A. Dey[9], M. Doi[10], M. Donahue[11], S. Deustua[12], P. Eisenhardt[13], E. Ellingson[14], L. Faccioli[1,2], V. Fadeyev[15], H. K. Fakhouri[1,2], A. S. Fruchter[12], D. G. Gilbank[16], M. D. Gladders[17], G. Goldhaber[1,2,42], A. H. Gonzalez[18], A. Goobar[4,19], A. Gude[2,20], T. Hattori[21], H. Hoekstra[22], E. Hsiao[1,2], X. Huang[1,2], Y. Ihara[10,43], M. J. Jee[23], D. Johnston[11,24], N. Kashikawa[25], B. Koester[17,26], K. Konishi[27], M. Kowalski[28], E. V. Linder[1,2], L. Lubin[23], J. Melbourne[29], J. Meyers[1,2], T. Morokuma[10,25,43], F. Munshi[2,30], C. Mullis[31], T. Oda[32], N. Panagia[12], S. Perlmutter[1,2], M. Postman[12], T. Pritchard[2,33], J. Rhodes[13,29], P. Ripoche[1,2], P. Rosati[34], D. J. Schlegel[1], A. Spadafora[1], S. A. Stanford[23,35], V. Stanishev[19,36], D. Stern[13], M. Strovink[1,2], N. Takanashi[25], K. Tokita[10], M. Wagner[37], L. Wang[38], N. Yasuda[39], and H. K. C. Yee[40]

(The Supernova Cosmology Project)

[1] E.O. Lawrence Berkeley National Lab, Berkeley, CA 94720, USA; nsuzuki@lbl.gov, rubind@berkeley.edu
[2] Department of Physics, University of California Berkeley, Berkeley, CA 94720, USA
[3] Australian Astronomical Observatory, Epping, NSW 1710, Australia; clidman@aao.gov.au
[4] The Oskar Klein Centre for Cosmo Particle Physics, AlbaNova, SE-106 91 Stockholm, Sweden
[5] Departamento de Astronomía y Astrofísica, Pontificia Universidad Católica de Chile, Santiago, Chile
[6] Harvard-Smithsonian Center for Astrophysics, Cambridge, MA 02138, USA
[7] Department of Physics, Hamilton College, Clinton, NY 13323, USA
[8] Department of Physics and Astronomy, University of Utah, Salt Lake City, UT 84112, USA
[9] National Optical Astronomy Observatory, Tucson, AZ 85726-6732, USA
[10] Institute of Astronomy, Graduate School of Science, University of Tokyo 2-21-1 Osawa, Mitaka, Tokyo 181-0015, Japan
[11] Department of Physics and Astronomy, Michigan State University, East Lansing, MI 48824, USA
[12] Space Telescope Science Institute, Baltimore, MD 21218, USA
[13] Jet Propulsion Laboratory, California Institute of Technology, Pasadena, CA 91109, USA
[14] Center for Astrophysics and Space Astronomy, 389 UCB, University of Colorado, Boulder, CO 80309, USA
[15] Santa Cruz Institute for Particle Physics, University of California Santa Cruz, Santa Cruz, CA 94064, USA
[16] Department of Physics and Astronomy, University Of Waterloo, Waterloo, ON N2L 3G1, Canada
[17] Department of Astronomy and Astrophysics, University of Chicago, Chicago, IL 60637, USA
[18] Department of Astronomy, University of Florida, Gainesville, FL 32611, USA
[19] Department of Physics, Stockholm University, Albanova University Center, SE-106 91 Stockholm, Sweden
[20] School of Physics & Astronomy, University of Minnesota, Minneapolis, MN 55455, USA
[21] Subaru Telescope, National Astronomical Observatory of Japan, Hilo, HI 96720, USA
[22] Leiden Observatory, Leiden University, Leiden, The Netherlands
[23] Department of Physics, University of California Davis, Davis, CA 95616, USA
[24] Department of Physics and Astronomy, Northwestern University, Evanston, IL 60208, USA
[25] National Astronomical Observatory of Japan, Tokyo 181-8588, Japan
[26] Kavli Institute for Cosmological Physics, The University of Chicago, Chicago, IL 60637, USA
[27] Institute for Cosmic Ray Research, University of Tokyo, Kashiwa 277-8582, Japan
[28] Physikalisches Institut Universität Bonn, Germany
[29] Caltech Optical Observatories, Division of Physics, Mathematics, and Astronomy, California Institute of Technology, Pasadena, CA 91125, USA
[30] Astronomy Department, University of Washington, Seattle, WA 98195, USA
[31] Wachovia Corporation, NC6740, Winston-Salem, NC 27101, USA
[32] Department of Astronomy, Kyoto University, Sakyo-ku, Kyoto 606-8502, Japan
[33] Department of Astronomy and Astrophysics, The Pennsylvania State University, University Park, PA 16802, USA
[34] ESO, D-85748 Garching, Germany
[35] Institute of Geophysics and Planetary Physics, Lawrence Livermore National Laboratory, Livermore, CA 94550, USA
[36] CENTRA-Centro Multidisciplinar de Astrofísica, Instituto Superior Técnico, 1049-001 Lisbon, Portugal
[37] Space Sciences Lab, University of California, Berkeley, CA 94720, USA
[38] Department of Physics, Texas A & M University, College Station, TX 77843, USA
[39] Institute for the Physics and Mathematics of the Universe, University of Tokyo, Kashiwa 277-8583, Japan
[40] Department of Astronomy and Astrophysics, University of Toronto, Toronto, ON M5S 3H4, Canada
Received 2011 February 15; accepted 2011 July 6; published 2012 January 27

ABSTRACT

We present Advanced Camera for Surveys, NICMOS, and Keck adaptive-optics-assisted photometry of 20 Type Ia supernovae (SNe Ia) from the *Hubble Space Telescope* (*HST*) Cluster Supernova Survey. The SNe Ia were discovered over the redshift interval $0.623 < z < 1.415$. Of these SNe Ia, 14 pass our strict selection cuts and are used in combination with the world's sample of SNe Ia to derive the best current constraints on dark energy. Of our new SNe Ia, 10 are beyond redshift $z = 1$, thereby nearly doubling the statistical weight of *HST*-discovered SNe Ia beyond this redshift. Our detailed analysis corrects for the recently identified correlation between SN Ia luminosity and host galaxy mass and corrects the NICMOS zero point at the count rates appropriate for very distant SNe Ia. Adding these SNe improves the best combined constraint on dark-energy density, $\rho_{\rm DE}(z)$, at redshifts $1.0 < z < 1.6$ by 18% (including systematic errors). For a flat ΛCDM universe, we find $\Omega_\Lambda = 0.729 \pm 0.014$ (68% confidence level (CL) including systematic errors). For a flat wCDM model, we measure a constant dark-energy equation-of-state

parameter $w = -1.013^{+0.068}_{-0.073}$ (68% CL). Curvature is constrained to ∼0.7% in the $o$$w$CDM model and to ∼2% in a model in which dark energy is allowed to vary with parameters w_0 and w_a. Further tightening the constraints on the time evolution of dark energy will require several improvements, including high-quality multi-passband photometry of a sample of several dozen $z > 1$ SNe Ia. We describe how such a sample could be efficiently obtained by targeting cluster fields with WFC3 on board *HST*. The updated supernova Union2.1 compilation of 580 SNe is available at http://supernova.lbl.gov/Union.

Key words: cosmological parameters – distance scale – supernovae: general

Online-only material: color figures, machine-readable table

1. INTRODUCTION

More than a dozen years have passed since combined observations of nearby and distant Type Ia supernovae (SNe Ia) demonstrated that the expansion of the universe is accelerating at the current epoch (Perlmutter et al. 1998, 1999; Garnavich et al. 1998; Schmidt et al. 1998; Riess et al. 1998). While the significance of the result has been boosted with the inclusion of larger, better calibrated SN Ia data sets (Knop et al. 2003; Astier et al. 2006; Wood-Vasey et al. 2007; Kowalski et al. 2008; Hicken et al. 2009b; Kessler et al. 2009; Guy et al. 2010), the cause of the acceleration remains unknown. Einstein's cosmological constant, for which w, the dark-energy equation-of-state parameter, is exactly -1 and independent of time, is just one of several possible explanations that is consistent with the constraints from SNe Ia and the constraints from other probes, such as the cosmic microwave background (CMB; Dunkley et al. 2009; Komatsu et al. 2011) and baryon acoustic oscillations (BAO; Eisenstein et al. 2005; Percival et al. 2010).

SNe Ia constrain cosmological parameters through the comparison of their apparent luminosities over a range of redshifts. At the highest redshifts, $z > 1$, the *Hubble Space Telescope* (*HST*) has played and continues to play a key role in discovering and confirming $z > 1$ SNe Ia (Riess et al. 2004, 2007; Kuznetsova et al. 2008; Dawson et al. 2009) and in providing high-precision optical and near-IR light curves. While constant w can be constrained using $z \sim 0.5$ SNe Ia, SNe Ia at $z > 1$ provide the necessary redshift baseline to constrain time-varying w and some astrophysical systematics like intergalactic dust (Ménard et al. 2010).

Discovering and following distant SNe Ia with *HST* requires substantial amounts of telescope time because its field of view is quite small compared to that of ground-based telescopes. Therefore, all *HST* SN Ia discovery programs have coupled the search for SNe Ia and their photometric follow-up with other scientific studies. The GOODS survey (Dickinson et al. 2003; Riess et al. 2004, 2007; Kuznetsova et al. 2008) is an example that provided a window to probe the high-z universe for studying galaxy evolution (e.g., Beckwith et al. 2006; Bouwens et al. 2006; Bundy et al. 2005) in addition to $z > 1$ SNe. Nevertheless, progress in building a large sample of $z > 1$ SNe Ia discovered with *HST* is slow. In the most recent SN Ia compilation (Union2; Amanullah et al. 2010) which consists of 557 SNe after the light-curve quality cuts, only 16 *HST*-discovered $z > 1$ SNe Ia were available to help constrain a time-evolving w. (Well-measured ground-based $z > 1$ SNe account for an additional four.)

Targeting regions that are rich in potential SN Ia hosts, such as galaxy clusters, offer a more effective strategy for using *HST* for SN Ia studies. Some of the earliest SN Ia searches used this strategy when the field of view of ground-based images was only a few arcminutes across. The first spectroscopically confirmed high-redshift SN Ia was discovered in a galaxy cluster (SN1988U: $z = 0.31$; Norgaard-Nielsen et al. 1989) as was the first high-redshift SN Ia observed by *HST* (SN1996cl: $z = 0.83$; Perlmutter et al. 1998, 1999). However, the advent of large-format CCDs, CCD mosaics, and imagers with wide fields of view quickly led away from this approach in the late 1980s and early 1990s (Perlmutter et al. 1991).

Given the large increase in the number of very distant clusters that have been discovered over the last 10 years, the angular extent of these clusters, and the field of view that is available with *HST*, targeting galaxy clusters beyond $z \sim 1$ is again an effective strategy. In this paper, we discuss results from our *HST* Cluster SN survey obtained using this strategy. In addition to increasing the yield of SNe Ia discoveries per *HST* orbit by a factor of two (Dawson et al. 2009), we increase the yield of SNe Ia in early-type galaxies by a factor of approximately four (Meyers et al. 2012).

SNe Ia hosted by early-type galaxies offer several potential advantages over SNe Ia found in a broader range of host types. Stars in early-type galaxies are considerably older and span a smaller mass range than stars in late-type hosts. This may lead to a more uniform progenitor population. Evidence for this can be seen in the distribution in light-curve widths. SNe Ia in early-type host galaxies follow a narrower distribution than SNe Ia in late-type galaxies (Hamuy et al. 1996, 2000; Riess et al. 1999; Sullivan et al. 2006). Interestingly, the relationship between SN Ia color and host galaxy type is weak (Sullivan et al. 2010). Using data from the *HST* Cluster SN Survey, we confirm both of these relationships for $z > 1$ SNe Ia in Meyers et al. (2012).

With the availability of larger, better-calibrated samples, evidence for a correlation between host galaxy properties and SN Ia luminosities after corrections for light-curve width and SN Ia color is now emerging. Hicken et al. (2009b) found that SNe Ia in early-type galaxies (morphologically classified as E and S0 galaxies) are 0.14 ± 0.07 mag brighter after light-curve shape and color corrections than SNe Ia in galaxies of later types. A relationship of roughly the same significance between host galaxy mass[44] and Hubble residuals was reported by Kelly et al. (2010), Sullivan et al. (2010), and Lampeitl et al. (2010). Uncorrected, this relationship leads to a significant systematic error in determining cosmological parameters, as the fraction of

* Based in part on observations made with the NASA/ESA *Hubble Space Telescope*, obtained from the data archive at the Space Telescope Institute. STScI is operated by the Association of Universities for Research in Astronomy, Inc., under the NASA contract NAS 5-26555. The observations are associated with program GO-10496.

[41] W. M. Keck Postdoctoral Fellow at the Harvard-Smithsonian Center for Astrophysics.

[42] Deceased.

[43] JSPS Fellow.

[44] Host galaxy metallicity, specific star formation rate, or age are also drivers, as these quantities are somewhat degenerate in current data.

SN Ia in galaxies with high specific star formation rates increases with increasing redshift (Sullivan et al. 2010). We expect that the host-mass correction is a proxy for more profound physics behind the SN Ia explosion mechanism; SNe Ia in early-type galaxies may lead to a better understanding of this correlation, given that more accurate mass, metallicity, and age can be assigned to early-type galaxies (Bruzual & Charlot 2003; Tremonti et al. 2004; Maraston 2005).

An additional source of astrophysical uncertainty concerns the color correction that is applied to SN Ia luminosities. There appear to be at least two mechanisms for the redder–fainter relation: extinction from dust in the interstellar medium, which must play a role at some level, and an intrinsic relation between color and luminosity due to the explosion itself or the surrounding environment. There is no reason to believe that the redder–fainter relationship should behave in the same way for both mechanisms at all redshifts, but the two effects have proven to be hard to disentangle.

Early-type galaxies contain significantly less dust than late-type galaxies, so separating SNe Ia according to early and late types offers a way to study the intrinsic component and to perhaps estimate the relative contribution and importance of dust in a broader sample. An early-type-only sample may also yield a Hubble diagram with smaller statistical errors. Early work, based on a few dozen SNe Ia without color correction, suggested that SNe Ia in early-type galaxies are better standard candles (Sullivan et al. 2003). The evidence from more recent works, which use larger samples and better data, revealed that SNe Ia exhibit intrinsic diversity in color, but support the original findings (Sullivan et al. 2003) with lower statistical significance (Sullivan et al. 2010).

Per unit stellar mass, SNe Ia are far less common in passive, early-type galaxies than in star-forming, late-type galaxies (Mannucci et al. 2005; Sullivan et al. 2006). Depending on the way hosts are classified, about one in five SNe Ia at low redshift will be hosted by an early-type galaxy. At higher redshifts, the fraction is expected to decrease due to a combination of an increase in the amount of star formation and observational selection biases. Galaxy clusters, which are rich in early-type galaxies, even up to $z \sim 1.4$, are an effective way of finding SNe Ia in early-type hosts (Dawson et al. 2009).

This paper is one of a series of 10 papers that report SN results from the *HST* Cluster Supernova Survey (PI: S. Perlmutter, GO-10496), a survey to discover and follow SNe Ia of very distant clusters. Paper I (Dawson et al. 2009) describes the survey strategy and discoveries. Paper II (Barbary et al. 2012a) reports on the SN Ia rate in clusters. Paper III (Meyers et al. 2012) addresses the properties of the galaxies that host SNe Ia. Paper IV (Ripoche et al. 2012) introduces a new technique to calibrate the "zero point" of the NICMOS camera at low count rates, which is critical for placing NICMOS-observed SNe Ia on the Hubble diagram. The current work, Paper V, reports the SN Ia light curves and cosmology from the *HST* Cluster SN Survey program. Paper VI (Barbary et al. 2012b) will report on the volumetric field SN Ia rate. Melbourne et al. (2007), one of several unnumbered papers in this series, present a Keck adaptive optics (AO) observation of a $z = 1.31$ SN Ia in H band. Barbary et al. (2009) report the discovery of the extraordinary luminous SN, SN SCP06F6. Morokuma et al. (2010) present the spectroscopic follow-up observations for SN Ia candidates. Hsiao et al. (2011) develop techniques to remove problematic artifacts remaining after the standard STScI pipeline. A separate series of papers, 10 to date, reports on cluster studies from the *HST* Cluster SN Survey: Brodwin et al. (2011), Eisenhardt et al. (2008), Jee et al. (2009, 2011) Hilton et al. (2007), Hilton et al. (2009), Huang et al. (2009), Santos et al. (2009), Strazzullo et al. (2010), and Rosati et al. (2009).

This paper is organized as follows. In Section 2, we describe the *HST* Cluster SN Survey, the search strategy and discuss SN Ia typing. In Section 3, we describe the procedures we used to process data and present the SN Ia photometry. In Section 4, we update the Union2 sample by adding the new SNe Ia from this paper and use the revised compilation to constrain cosmological parameters in Section 5.

2. SN DISCOVERIES AND DATA

The *HST* Cluster Supernova Survey targeted 25 high-redshift galaxy clusters in the redshift range $0.9 < z < 1.5$ with the Advanced Camera for Surveys (ACS) camera on board *HST*. Clusters were selected from the IRAC Shallow Cluster Survey (Eisenhardt et al. 2008), the Red-Sequence Cluster Surveys (RCS and RCS-2; Gladders & Yee 2005; Gilbank et al. 2011), the *XMM* Cluster Survey (Sahlén et al. 2009), the Palomar Distant Cluster Survey (Postman et al. 1996), the *XMM-Newton* Distant Cluster Project (Bohringer et al. 2005), and the *ROSAT* Deep Cluster Survey (RDCS; Rosati et al. 1999). At the time we conducted our survey, the sample represented a significant fraction of the known $z > 0.9$ clusters. Here, we summarize the SNe discovered in our survey.

2.1. SN Sample

As described in Dawson et al. (2009), the survey produced a total of 39 likely SNe during the active phase of the search. In Barbary et al. (2012a), types are determined for 29 of these candidates. (The remaining 10 do not have enough light-curve information to determine their types, since they lie outside of our fiducial search time window or our signal-to-noise cuts.) Twenty SNe are classified as SNe Ia, with confidence levels (CL) of secure, probable, or plausible. A secure SN Ia is one that either has a spectrum that directly confirms it to be an SN Ia *or* one that satisfies two conditions: (1) it occurred in a host whose spectroscopic, photometric, and morphological properties are consistent with those of an early-type galaxy with no detectable signs of recent star formation, and (2) it has a light-curve shape consistent with that of an SN Ia and inconsistent with all other known SN types. A probable SN Ia is one that does not have a secure spectrum but satisfies one of the two non-spectroscopic conditions that are required for a secure classification. A plausible SN Ia is one that has an indicative light curve but we do not have enough data to rule out other types. Details of the classification scheme can be found in Barbary et al. (2012a) and details of the galaxy typing can be found in Meyers et al. (2012).

Sixteen SNe are classified as either secure or probable. We use these SNe in the cosmological analysis. We include the photometry and light curves of an additional four plausible SNe Ia to illustrate the quality of the data and the potential for a similar sample with complete classification (and because additional host galaxy data may later bring one of these into the larger sample). Secure, probable, and plausible SN Ia are listed in Table 1, together with their position, redshift, and typing. Postage stamp images of the SNe and host galaxies are shown in Figure 1.

We labeled each of our 25 clusters with a letter from "A" to "Z" (excluding "O" to avoid confusion with zero) and

Table 1
Supernova from the *HST* Cluster Supernova Survey

SN Name	Nickname	z[a]	$z_{\rm cluster}$[b]	R.A. (J2000)	Decl. (J2000)	$E(B-V)$[c]	Confidence
SNe Hosted by Cluster Early-type Galaxies							
SCP05D0[d]	Frida	1.014	1.017	02:21:42.066	−03:21:53.12	0.025	Secure
SCP06H5	Emma	1.231	1.241	14:34:30.140	+34:26:57.30	0.019	Secure
SCP06K0	Tomo	1.415	1.414	14:38:08.366	+34:14:18.08	0.015	Secure
SCP06K18	Alexander	1.411	1.414	14:38:10.665	+34:12:47.19	0.014	Probable
SCP06R12	Jennie	1.212	1.215	02:23:00.083	−04:36:03.05	0.026	Secure
SCP06U4[d]	Julia	1.050	1.037	23:45:29.430	−36:32:45.75	0.014	Secure
SNe Hosted in the Cluster							
SCP06C1[d]	Midge	0.98	0.974	12:29:33.013	+01:51:36.67	0.019	Secure
SCP06F12	Caleb	1.110	1.110	14:32:28.749	+33:32:10.05	0.010	Probable
SNe Hosted by Early-type Non-cluster Members							
SCP05D6	Maggie	1.315	1.017	02:21:46.484	−03:22:56.18	0.025	Secure
SCP06G4[d]	Shaya	1.350	1.259	14:29:18.744	+34:38:37.39	0.015	Secure
SCP06A4	Aki	1.192	1.457	22:16:01.078	−17:37:22.10	0.026	Probable
SCP06C0	Noa	1.092	0.974	12:29:25.655	+01:50:56.59	0.020	Secure
SNe Hosted by Late-type Galaxies							
SCP06G3	Brian	0.962	1.259	14:29:28.430	+34:37:23.15	0.015	Plausible
SCP06H3[d]	Elizabeth	0.850	1.241	14:34:28.879	+34:27:26.62	0.019	Secure
SCP06N33	Naima	1.188	1.026	02:20:57.699	−03:33:23.98	0.023	Probable
SCP05P1	Gabe	0.926	1.1	03:37:50.352	−28:43:02.67	0.011	Plausible
SCP05P9[d]	Lauren	0.821	1.1	03:37:44.513	−28:43:54.58	0.011	Secure
SCP06X26	Joe	1.440	1.101	09:10:37.888	+54:22:29.06	0.019	Plausible
SCP06Z5[d]	Adrian	0.623	1.390	22:35:24.967	−25:57:09.61	0.021	Secure
SNe with No Definitive Redshift Measurement							
SCP06E12	Ashley	···	1.026	14:15:08.141	+36:12:42.93	0.009	Plausible

Notes.
[a] Redshift from SNe Ia or host galaxy (Morokuma et al. 2010; Barbary et al. 2012a; Meyers et al. 2012).
[b] Redshift from cluster (Meyers et al. 2012 and references therein).
[c] Galactic Extinction from Schlegel et al. (1998).
[d] Spectroscopically confirmed as SNe Ia.

assigned SN names as "SCP"+[discovery year]+ [discovered cluster]+[SN ID]. The cluster IDs, coordinates, and redshifts are found in tables in Dawson et al. (2009), Barbary et al. (2012a), and Meyers et al. (2012). The cluster membership is discussed in detail in Meyers et al. (2012) and summarized in Table 1 along with host type information.

Several SNe Ia deserve special mention.

SN SCP06C1, an SN discovered in 2006 in cluster C (XMMU J2205.8−0159) and numbered as "1" among other transient candidates, could not be clearly associated with a galaxy in the cluster but was spectroscopically confirmed as an SN Ia at the cluster redshift. It might be an example of an SN Ia that comes from a progenitor in the intracluster stellar population (Sand et al. 2011). SN SCP06C1 is discussed in greater detail in Barbary et al. (2012a). As there was a bright background galaxy near the position of the SN, had we not obtained a spectrum of the SN, we would have misidentified the redshift. We note that experiments that do not obtain spectroscopy of their SNe and instead assume the nearest visible galaxy is the host will have to factor cases like SN SCP06C1 into their analyses.

SN SCP05D6, SN SCP06G4, and SN SCP06N33 occur behind the cluster and are therefore gravitationally lensed by the cluster. In most surveys, the lensing for SNe Ia hosted by field galaxies averages to nearly zero. In this survey, we target regions with larger than average magnification, so we must make the correction for SNe behind the clusters. To estimate the amount of magnification, we use the virial mass, M_{200}, from our weak lensing measurements (Jee et al. 2011). We assume a spherical Navarro–Frenk–White profile (Navarro et al. 1997) with the concentration parameters determined by the M_{200}–c relation in Duffy et al. (2008). The lensing magnifications for SN SCP05D6, SN SCP06G4, and SN SCP06N33 are estimated to be $1.021^{+0.012}_{-0.008}$, $1.015^{+0.005}_{-0.004}$, and $1.066^{+0.017}_{-0.014}$, respectively. The magnification of SN SCP06N33 is larger than the others because the cluster is massive and the host galaxy is located at approximately half the distance from cluster center as the others. We apply these corrections when using these SNe Ia in the cosmological fits and propagate the uncertainties accordingly.

SN SCP06C0 is a more interesting case. The host is also behind the lensing cluster, which means that SN SCP06C0 will be lensed as well. Following the methodology used to correct SN SCP06G4, SCP SN05D6, and SCP SN06N33, we find the magnification of SN SCP06C0 to be $1.030^{+0.007}_{-0.005}$. Upon closer inspection of the host in the stacked ACS data and in more recent WFC3 data, a second, much fainter object, projected only 0.″6 from the center of the host and about 0.″2 from SN SCP06C0, was detected. The object could be a satellite of the host, or it could be an unrelated galaxy along the line of sight. A spectrum of SN SCP06C0 was taken when it was about six days after maximum light; however, the signal-to-noise ratio was insufficient to allow a clear detection of light from the SN given the observing conditions and the relative brightnesses of the hosts and the SN. The classification and redshift therefore rely on correctly assigning the SN to the brighter galaxy. In

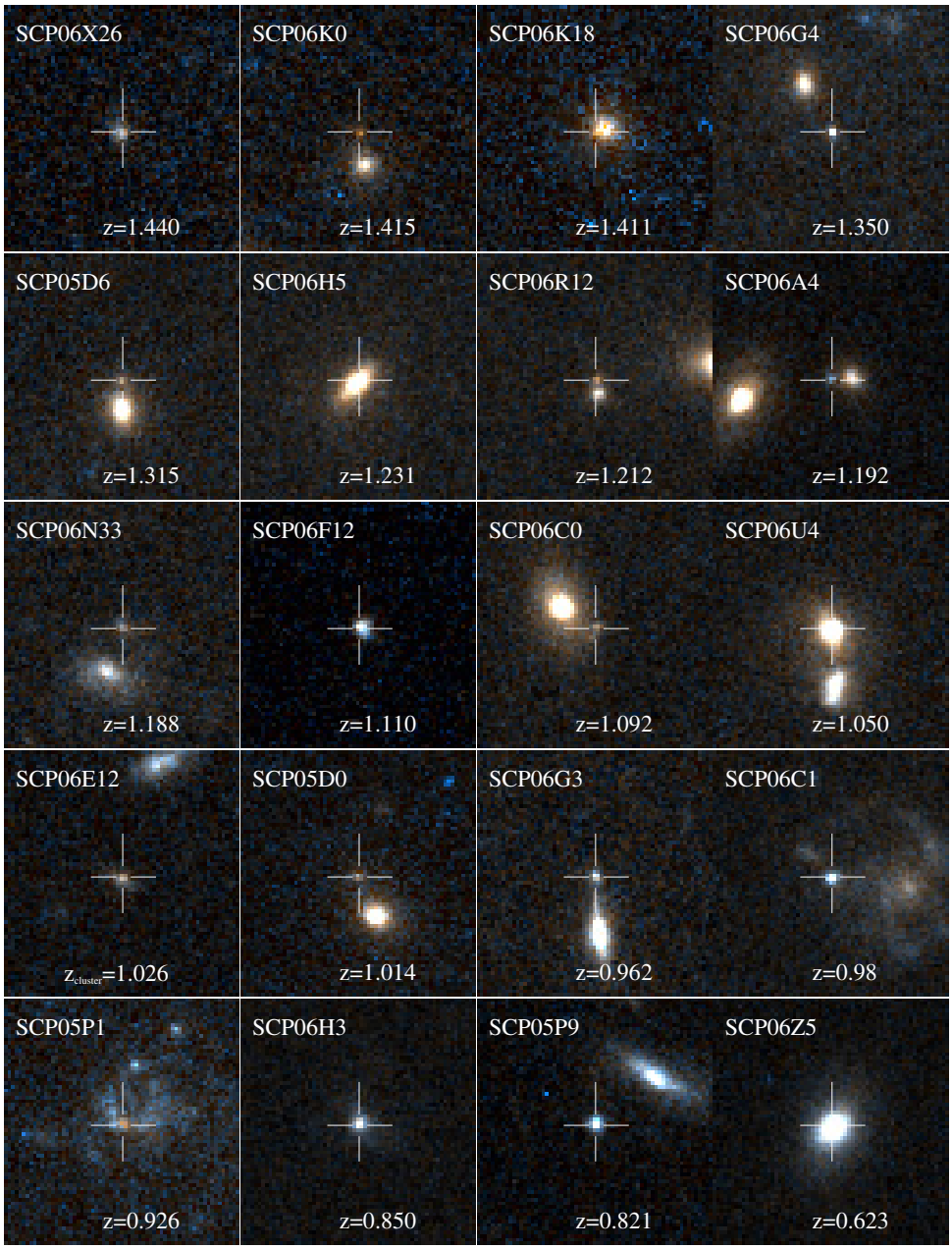

Figure 1. Composite color (i_{775} and z_{850}) images of 20 SNe Ia from the *HST* Cluster Supernova Survey. Each SN Ia is shown in a box of $3\farcs2 \times 3\farcs3$ (north is up and east is left). Note that the redshift of SCP06E12 is uncertain, and we use the cluster redshift as a guide.

Section 3.2.3, we model the surface brightness distribution of both galaxies. At the location of the SN, the surface brightness of the large galaxy is four times greater than the surface brightness of the small galaxy. Since [O II] was not detected in spectra that were taken after the SN had faded from view, neither galaxy is actively forming stars. The relative SN rate is therefore directly related to the relative surface mass density of the two galaxies. Using the surface brightness as a proxy for the surface mass density, we therefore assign SN SCP06C0 to the larger of the two galaxies with ∼80% confidence and include this SN Ia in the cosmological fits.

3. PHOTOMETRY

In this section, we describe the steps that were used to process the ACS and NICMOS data after they had been processed with the standard STScI pipelines. For the ACS data, we removed the spatially variable background from the pipeline processed data and applied charge transfer efficiency (CTE) and red-halo scattering corrections to the extracted fluxes. For the NICMOS data, we processed the data to compensate for amplifier offsets, bright Earth persistence, contamination from the passage of the telescope through the South Atlantic Anomaly (SAA), residual amplifier glow and fringing, and applied a wavelength-dependent nonlinearity correction. A more detailed description of the individual steps now follows.

3.1. ACS Processing and Photometry

In general, the search consisted of four z_{850} exposures per epoch and a single i_{775}-band exposure. All exposures are geometrically corrected (and multiple exposures are stacked) using MultiDrizzle (Fruchter & Hook 2002; Koekemoer et al. 2002). The photometry is performed on the stacked z_{850}-band

Table 2
Photometry Data

SN Name	Instrument	Filter	MJD	Flux[a] (counts s^{-1})	Flux Error[a] (counts s^{-1})	Vega Zero Point	Exptime (s)	N_{exp}[b]	Raw Flux[c] (counts s^{-1})	Raw Flux Error[c] (counts s^{-1})
SCP05D0	ACS	F850LP	53564.098	−0.0283	0.0547	24.371	2000	4	−0.0188	0.0365
SCP05D0	ACS	F850LP	53589.117	0.7733	0.0573	24.371	2000	4	0.5153	0.0381
SCP05D0	NICMOS	F110W	53604.074	0.5092	0.0230	23.029	2560	2	...	...
SCP05D0	ACS	F850LP	53610.836	1.5084	0.0649	24.371	2000	4	1.0040	0.0432
SCP05D0	ACS	F850LP	53633.184	0.7290	0.0704	24.371	1500	4	0.4764	0.0460
SCP05D0	ACS	F775W	53633.215	0.7989	0.2229	25.315	375	1	...	...
SCP05D0	ACS	F850LP	53654.434	0.2388	0.0694	24.371	1500	4	0.1520	0.0442
SCP05D0	ACS	F775W	53654.469	0.3908	0.1725	25.315	375	1	...	...
SCP05D0	ACS	F850LP	53679.258	0.1792	0.0708	24.371	1500	4	0.1137	0.0450
SCP05D0	ACS	F775W	53679.273	−0.1432	0.1823	25.315	375	1	...	...
SCP05D0	ACS	F850LP	53704.266	0.0279	0.0715	24.371	1500	4	0.0174	0.0446
SCP05D0	ACS	F775W	53704.305	0.0624	0.2072	25.315	375	1	...	...
SCP05D0	ACS	F850LP	53965.207	0.0356	0.0738	24.347[d]	1360	4	0.0216	0.0448
SCP05D0	ACS	F775W	53965.246	−0.0034	0.1981	25.301[d]	515	1	...	...

Notes.
[a] Flux, corrected for CTE and color-dependent aperture correction (for ACS) and the count-rate nonlinearity (for NICMOS). For the ACS F850LP filter, z_{850}, this is the result of the iterative Method I in the Appendix.
[b] The number of exposures.
[c] CTE-corrected but not aperture-corrected flux for the ACS F850LP data. This flux column is used as an input for the modified filter Method II in the Appendix. Note we use the modified filter response curve and shifted zero point as described in the Appendix.
[d] The zero point has changed slightly after 2006 July 4 (MJD = 53920) due to the change in detector temperature.

(This table is available in its entirety in a machine-readable form in the online journal. A portion is shown here for guidance regarding its form and content.)

image and the single i_{775}-band drizzled image. In addition to the data that were taken during the search, five clusters, CL1604+4304 (Postman et al. 2005), RDCS0910+54 (Mei et al. 2006), RDCS0848+44 (Postman et al. 2005), RDCS1252−29 (Blakeslee et al. 2003), and XMMU 2235.3−2557 (Jee et al. 2009), were observed with ACS prior to our program (PID9290 and PID9919). We have included all of these data and processed them and the search data in a uniform way. In total, 1006 ACS exposures were processed.

After processing the ACS data with the standard STScI pipeline using the most up-to-date calibration files, we removed the spatially variable background by masking all objects and artifacts, and subtracting a heavily smoothed, median version of what remained. Given the time baseline of our observations, guide stars changed between epochs. We must therefore use objects in the images—typically 20–30 objects per image—to tie the relative astrometry between epochs. The size of the residuals was typically 0.2 pixels, which is larger than one usually expects from point sources with good signal-to-noise ratios. We attribute this to temporal and spatial uncertainties in the distortion correction that are applied to images that are both temporally separated by many months and rotated with respect to one another (Anderson 2007). The absolute astrometry is tied to the Guide Star Catalogue, version 2.3.2,[45] and has an uncertainty of 0.″3.

We use apertures of 3 pixel radius to measure fluxes and report the i_{775} and z_{850} photometry for each epoch of each SN in the online version of this paper. An example is shown in Table 2. The background noise is found empirically by randomly placing apertures within regions that are free of objects and then measuring the dispersion in the integrated counts within these apertures. We have compared the signal-to-noise ratios obtained for aperture and point-spread function (PSF) photometry and found that the difference between the two is small if we use such small apertures. We use aperture photometry here, as it allows for a more robust correction of CTE and red-halo scattering (described below).

The photometry is corrected for variable CTE and for flux that is outside the aperture (referred to here as the aperture correction (AC)). CTE depends on the position of the source, the level of the background sky, and the flux of the object that is being corrected. It also degrades with time. We follow the formulation of Riess & Mack (2004) and apply the correction factor that corresponds to the 3 pixel radius case and the dates of our observations. On average, we applied a 4.3% correction to the SN Ia flux. When calculating CTE corrections, we include the local background that had been previously subtracted.

We also apply a color-dependent AC on the ACS z_{850}-band measurements. In the ACS z_{850}-band data, long-wavelength photons scatter off the back side of the CCD, causing a degradation in the PSF. The effect is commonly known as red-halo scattering (Sirianni et al. 1998). The TinyTim[46] PSF does not account for this effect, and hence it does not reproduce the observed z_{850}-band PSF. We studied how the PSF changes with wavelength using standard stars taken with a series of narrowband filter observations from the *HST* calibration programs PID9020 and PID10720. We measured the red-halo scattering correction factor as a function of aperture radius and wavelength. For a given aperture, we then can treat the correction as a modification of the F850LP throughput and zero point. We discuss the details of this procedure in the Appendix.

We have used the updated STScI ACS Vega zero points for light-curve fitting. The latest zero points are from the STScI web site[47] which were posted on 2009 May 19. The ACS zero points changed on 2006 July 4 due to a change in the detector temperature. The STScI definition assigns Vega (α Lyr) a magnitude of 0.0 in every filter. However, in the

[45] http://gsss.stsci.edu/Catalogs/GSC/GSC2/gsc23/gsc23_release_notes.htm
[46] http://www.stsci.edu/software/tinytim/tinytim.html
[47] http://www.stsci.edu/hst/acs/analysis/zeropoints

Landolt system, to which the SN Ia photometry in the literature refers, Vega is not zero. To be consistent with the literature about SNe Ia, we introduce this non-zero Vega magnitude correction to our zero points. For both the i_{775} and z_{850} bands, the correction is 0.024 mag (Fukugita et al. 1996). We therefore adjust the STScI zero points by this amount (Astier et al. 2006) and use "non-zero Vega magnitude" system zero points of $i_{775} = 25.291(\mathrm{STScI}) + 0.024 = 25.315$ and $z_{850} = 24.347(\mathrm{STScI}) + 0.024 = 24.371$ for data taken before 2006 July (corresponding to a detector temperature of -77°C), and $i_{775} = 25.277(\mathrm{STScI}) + 0.024 = 25.301$ and $z_{850} = 24.323(\mathrm{STScI}) + 0.024 = 24.347$ for data taken after 2006 July (corresponding to a detector temperature of -81°C).

3.2. NICMOS Processing and Photometry

All NICMOS science frames were processed with the latest CALNICA pipeline (version 4.4.1; Dahlen et al. 2008). This pipeline includes accurate weighting of each readout and optimal removal cosmic rays, as recommended in Fadeyev et al. (2006). CALNICA does not account for the effect of cosmic-ray hits on neighboring pixels (Fadeyev et al. 2006), but these were found to have no appreciable impact for the data reported here. Subsequently, the science frames were corrected for three well-known anomalies: the offset between amplifiers, which affects all NICMOS exposures and is removed using the STSDAS PyRAF task PEDSKY; persistence after the passage of the telescope through the SAA; and persistence after exposing the detectors to the limb of the Earth. Nine exposures are affected by the SAA, which leaves persistent signals from SAA cosmic rays. We applied the STSDAS PyRAF task SAACLEAN (Barker et al. 2007) to remove SAA persistence effects from the images. When a NICMOS observation is immediately preceded by an ACS data dump, the process could delay the NICMOS placement of the filter blank, subjecting the detectors to the bright limb of the Earth, which imprints a persistent pattern on subsequent exposures (Riess & Bergeron 2008). Four exposures were affected in this way and were corrected using the STSDAS software NIC_REM_PERSIST. At this point, the mode of the flux distribution in each image is measured and recorded. These values are used as the sky levels for the count-rate nonlinearity correction.

Even after correcting NICMOS data for these well-studied anomalies, significant large-scale background non-uniformities remain. We developed methods to extract and remove the background structures; these are detailed in Hsiao et al. (2011). Briefly, the models for the background structures are studied and characterized using approximately 600 NICMOS exposures observed through the F110W filter and processed with the procedures described above. Principal component analysis applied to these images revealed that the intensity of the residual corner amplifier glow depends on the exposure sequence. The amount of residual glow decays exponentially and resets every orbit. With exposure times on the order of 1000 s, the exposures can be separated into two glow groups, each with approximately constant intensity. This makes it possible to extract the residual glow algebraically. The structured background is modeled as a combination of a constant component and a component that scales with the sky level and exposure time. The models are derived from the algebraic manipulation of stacked images for each glow group. The resulting constant component of the model is dominated by residual amplifier glow at the corners and residual persistent structure at the center. The model component which scales with sky level and exposure time displays a curious fringe pattern whose origin is unknown. The model components are fit to individual exposures via scale parameters to create the customized background models to be subtracted from the individual exposures. In a final step, the bias offsets apparent in the middle column and middle row are removed. Additional details can be found in Hsiao et al. (2011).

3.2.1. NICMOS Count-rate Nonlinearity

The NICMOS data are critically important for measuring the color of $z > 1$ SNe Ia. Any uncertainty in the NICMOS calibration severely limits the usefulness of SNe Ia observed with NICMOS. In particular, the NIC2 detector exhibits a count-rate-dependent nonlinearity (Bohlin et al. 2005), the severity of which is a function of wavelength.

This nonlinearity has previously only been studied at count rates three orders of magnitude higher (de Jong et al. 2006) than the count rate of a typical SN Ia at $z = 1$, meaning that correcting the flux of SN Ia at $z = 1$ requires significant extrapolation and has a level of uncertainty that is difficult to quantify. For example, comparisons between ground-based near-IR data and a different NICMOS camera (NIC3) showed that little or no correction is required for that camera (Mobasher & Riess 2005). It is difficult to reconcile this finding with the findings of Bohlin et al. (2006) and de Jong et al. (2006). A simple test at the flux levels relevant for the SNe in this paper shows a difference of 12% between NIC2 and NIC3 when the nonlinearity corrections are made, revealing significant problems with these extrapolations.

For the NIC2/F110W filter, the degree of count-rate nonlinearity is $\sim$0.06 mag per factor of 10 change in count rate (Bohlin et al. 2006; de Jong et al. 2006). The count rates from stars that are used to determine the NICMOS zero points are five orders of magnitude higher than the count rate of a typical SN Ia at $z = 1$. This corresponds to a $\sim$0.3 mag correction for the NIC2/F110W filter.

Since this is so important to the cosmological results, we have developed a method to address this count-rate nonlinearity calibration directly (Ripoche et al. 2012). We analyze ACS, NICMOS, and ground-based near-IR observations of early-type galaxies from clusters RCS J0221.6−0347 ($z = 1.02$), RDCS J1252.9−2927 ($z = 1.24$), and XMMU J2235.3−2557 ($z = 1.39$). The space- and ground-based data are used to constrain the spectral energy distributions (SEDs) of these galaxies, which are then numerically integrated through the F110W filter transmission curve and compared to the counts measured with NICMOS. The principal advantage of the technique is that the count rate from early-type galaxies at this redshift is similar to that measured for SNe Ia, i.e., about 0.03 counts s^{-1} pixel^{-1} (the contribution from amplifier glow is comparable). We applied this technique using three galaxy clusters that have deep ground-based near-IR imaging data from the Very Large Telescope (VLT) and deep images with the ACS and NICMOS camera. All three clusters are at different redshifts and produced consistent results. At the low count rates that are applicable to high-redshift SNe Ia, we find that the prescription of Bohlin (2007) and de Jong et al. (2006) overpredicts the zero-point correction for the NIC2 camera with the F110W filter by 0.065 mag. We therefore use our zero point of 23.029 (Vega magnitude) or 23.757 (AB magnitudes). Additional details can be found in Ripoche et al. (2012).

At high count rates, the count-rate nonlinearity size has a strong dependence with wavelength across filters (de Jong et al. 2006), being considerably stronger in bluer filters. The SED of

an early-type galaxy at $z \sim 1.2$ is a good match to an SN Ia about 20 rest-frame days after maximum, but is redder than an SN SED at maximum (though this is compensated somewhat by the fact that the background level is about one-third of the source flux and is blue in the F110W bandpass). The size of the count-rate nonlinearity correction will thus also depend weakly on the phase and redshift, varying from 0.02 mag at maximum to no additional correction 20 rest-frame days after maximum. Since the wavelength dependence of the nonlinearity may not be even this strong at low count rates, we apply half the correction applicable at each phase and add (in quadrature) an additional 0.01 mag to the F110W zero-point error to account for this uncertainty. When added to the 0.006 mag statistical error, and 0.021 mag systematic error (Ripoche et al. 2012), this gives a total uncertainty on the zero point of 0.024 mag. For the GOODS SNe with NICMOS observations, we start with the original flux given by Riess et al. (2007; after converting the magnitude measurements to fluxes using the given zero point of 22.92), but increase the flux by 0.01 mag, representing half the correction for the (possible) wavelength dependence of the count-rate nonlinearity.

3.2.2. Galaxy Models

After the postprocessing described above (Hsiao et al. 2011), we measure fluxes from the eight SNe Ia with NICMOS observations by performing PSF photometry on the images. In all cases, the SNe Ia are not separated enough from their hosts to allow us to fit for the SN flux alone; rather we fit a model of the host galaxy as well. By performing PSF photometry using analytic galaxy models, we avoid resampling the images (the better PSF sampling for the ACS data negates this advantage of PSF photometry) and extract the maximum possible signal-to-noise from our observations. We fit an analytic model of the host galaxy even when we have reference images, as this gives higher signal-to-noise, and nearly uncorrelated photometry between epochs.[48]

Model PSFs for the SNe are obtained with the TinyTim software using SN SED templates from Hsiao et al. (2007) redshifted to the SN redshift and warped as a function of wavelength to match the photometry. After the light-curve fitting is complete, new PSFs are generated from the SEDs based on this photometry and the process is repeated. Model PSFs for the galaxies are obtained with TinyTim by appropriately redshifting a galaxy spectrum from Bruzual & Charlot (2003) with an age of 2.5 Gyr and a solar metallicity; the exact shape of the galaxy spectrum does not greatly affect the results. The PSFs used are 3″ in diameter, comparable to the patch fit in each NICMOS image.

Although there is virtually no information at scales smaller than about half a pixel, all PSFs are seven-times oversampled. This oversampling is necessary because the PSF is made slightly wider by the convolution with the subsampled pixels, increasing the flux of the derived photometry. In order for this effect to be negligible, seven-times oversampling must be used. Finally, a correction is made to match the photometry from the 3″ TinyTim PSFs to the 30″ TinyTim PSFs used in Ripoche et al. (2012). These differently sized PSFs show different structure far in the wings, but the flux in the core changes by 3.5%, with negligible variation.

[48] Had we subtracted the flux in the reference images at the location of the supernova, the errors from this flux would have to be propagated as a covariance for all the other epochs. The errors on the galaxy model at the position of the supernova are typically much smaller.

We generally model the host galaxies as ellipsoids, with radial profiles given by second degree polynomial splines. These splines have 10 nodes, with spacing that asymptotically approaches an exponential away from the core. The higher node density near the core provides more freedom to model the host where the flux changes quickly with position. In the few pixels closest to the core where the spline changes rapidly we numerically integrate over each subpixel before convolving with the PSF. On the basis of our tests (see Section 3.2.3), the hosts of some SNe were modeled with modifications to this basic scheme, as discussed in the following section.

3.2.3. Photometry Testing

Three ingredients all have to be correct in order to achieve photometry with low bias and variance: the PSF model, the galaxy model, and the SN centroid. Deriving a PSF from a field star (details in the SN SCP06C0 discussion below) and comparing with TinyTim gives photometry consistent to a few mmags, so we do not believe this is a major contribution to our errors.

Testing the host galaxy model and SN centroiding is more involved. For each observation, we subtract the best-fit SN light and place simulated SNe (at the same flux level) in the images. The only place one cannot do this test is at the location of the actual SN, as putting a simulated PSF in this location yields a measurement that will be highly correlated with the measurement of the SN. We therefore do not place any simulated SNe closer than two pixels to the best-fit location of the SN. By examining the bias and variance of the extracted fluxes from a large number of simulations (∼100), we can choose the galaxy model that gives the most precise and accurate[49] fluxes for each particular SN. We emphasize that the results of these simulations were the only metric used in choosing the detailed model. In particular, there was no feedback from the shape of the light curve or the Hubble diagram since these would have undercut the principles of "blind" analysis we tried to maintain (see Section 4). The same basic galaxy model (discussed above) was used for the NICMOS photometry of each SN, with the following exceptions.

1. *SN SCP06C0*. As mentioned in Section 2.1, there is a small galaxy about 0.″6 from the likely host of SN SCP06C0 and just 0.″2 from SN SCP06C0 itself. We note that the surface brightness of the small galaxy is one-fourth of that host at the location of the SN. The host also has some azimuthal asymmetry visible, indicating a possible merger. The cluster XMM1229+01 was also observed as part of a program to cross-calibrate NICMOS (P. Ripoche et al. 2012, in preparation) and deep, well-dithered images were obtained in the WFC3 F110W filter, allowing a more flexible background model to subtract both galaxies. We modeled the galaxies with a two-dimensional second-order spline, with nodes placed in a grid every 0.″076 (the natural pixel scale of NICMOS). The WFC3 F110W PSF was modeled as a combination of the elliptical galaxy model and a two-dimensional spline (with a spacing of 0.″1) using dithered images of a field star. (This is the same empirical PSF model used for testing TinyTim for NICMOS, although there the two-dimensional spline nodes are spaced at the natural pixel scale of NICMOS.) Our testing indicates that this method achieves the same signal-to-noise ratio as the other SNe that have simpler galaxy subtractions.

[49] We found that precision and accuracy correlated in our simulations.

2. *SN SCP06A4*. We found a small amount of azimuthal asymmetry in the host. Adding a second-order two-dimensional spline to the galaxy model, with a node spacing of 0.″38 (five times the natural pixel scale of NICMOS 2) successfully modeled this asymmetry, without adding additional measurement uncertainty to the SN flux.
3. *SN SCP05D6*. The host galaxy requires two elliptical components to be fitted well. These components are forced to have the same centroid, but are allowed different orientations, ellipticities, and radial profiles. One component forms a bulge, while the other one forms a disk. In one epoch contaminated by the SAA, aperture photometry with a 1 pixel radius aperture on the galaxy-model-subtracted images gave better signal-to-noise than PSF photometry, so we used this instead.
4. *SN SCP06U4*. This SN was on the core of a galaxy that appears to be merging with another galaxy. Similar to SN SCP05D6, a second elliptical component was needed to model the host (in this case, a third, detached component was used to model the fainter companion). Our simulated SNe revealed that, rather than using one host galaxy model to extract photometry, even more precise results were obtained averaging photometry results derived using the elliptical model and the two-dimensional spline model (discussed above for SN SCP06C0). Using this procedure results in a change in flux well inside the error bar.
5. *SN SCP06H5*. The one NICMOS observation of this SN was our most challenging extraction. The observation of the SN was 11 rest-frame days after maximum, and it is only ∼0.″1 from the core. As with SN SCP05D6, the host galaxy requires two elliptical components to be fitted well. (Comparing to the two-dimensional spline model discussed above, we obtain photometry that is the same to within a small fraction of the error bar.)
   The signal-to-noise ratio of this measurement is low, likely implying some amount of bias due to centroiding error. However, this is the only measurement with a signal-to-noise ratio this low, so no correlation is introduced with any other measurement.

3.3. Keck AO Photometry

The photometry of $z > 1.2$ SNe has been almost exclusively measured from *HST* images (Knop et al. 2003; Riess et al. 2004, 2007; Amanullah et al. 2010). At these redshifts, the rest-frame *B* band is redshifted beyond 9000 Å and falls in the near-IR (NIR). NIR observations are typically much easier from space, not only because of the higher spatial resolution of *HST* compared to ground-based seeing-limited systems, but also because of the lower NIR sky noise in space. However, we show here that AO on large ground-based telescopes can overcome these limitations and allow high-z SNe to be studied from the ground.

We observed the $z = 1.315$ SN SCP05D6 with the Keck Laser Guide Adaptive Optics (LGS AO) system. These observations were made in the *H* band (1.6 μm), which corresponds to the rest-frame *R* band. The diffraction-limited resolution of the Keck AO images was ∼0.″05, or a factor of three better than the spatial resolution of *HST* at these wavelengths. The high spatial resolution meant a much better separation of the SN from the galaxy core compared to *HST*. It also allowed greater contrast between the SN and the sky background. We obtain a photometric precision of 0.14 mag at $H \sim 24$ mag in a 1 hr exposure with Keck AO, showing the potential of AO in SN Ia cosmology.

Melbourne et al. (2007) report the details of the Keck AO photometry; here we briefly summarize the observations. The Keck LGS AO observing runs for the Center for Adaptive Optics Treasury Survey (Melbourne et al. 2005) coincided with the *HST* Cluster SN Survey program, and we successfully observed SN SCP05D6 at three epochs, before, near, and after the light-curve maximum.

A 14 mag star 25″ away was chosen to provide AO tip-tilt correction. The ∼11 mag sodium LGS was pointed at the galaxy to provide higher-order AO corrections. The observations were sampled with a 0.″01 pixel scale, allowing the diffraction-limited Keck PSF to be fully resolved. Individual exposures of 60 s were taken with five dithered pattern positions. The sequence was repeated until sufficient depth was reached. Total exposure times varied from 30 minutes to 1 hr per epoch.

We were also fortunate to have a 17.9 mag natural PSF star only 4″ away from SN SCP05D6, so the PSF near the location of the SN was well determined. From the star, we measured an FWHM of 0.″055 while we had a mean *H*-band seeing of 0.″4. Using the observed PSF, the host galaxy was modeled by GALFIT (Peng et al. 2002) and subtracted from the image, providing a clean measurement of the SN diffraction-limited core. Relative photometry with respect to the nearby PSF star was performed at each epoch and calibrated by the UKIRT standard star FS6 (the photometry is reported in Table 2). The photometric uncertainty was estimated by simulations of model PSFs embedded into the AO image at the same galactocentric radius as the actual SN.

We fit the SN light curve with the photometric data from *HST*/ACS F775W, F850LP, *HST*/NICMOS F110W, and this Keck/AO observation. We found that the Keck AO data were consistent with the *HST* observations (Figure 2). Although the uncertainty in the AO measurement was larger than that of *HST*, including it reduces the color uncertainty by more than 10%, and reduces the sensitivity of the fit to the NICMOS zero-point uncertainty by more than a one-third.

4. AUGMENTING THE UNION2 SUPERNOVA COMPILATION: UNION2.1

SNe Ia are an excellent probe of dark energy as they measure the magnitude–redshift relation with very good precision over a wide range of redshifts from $z = 0$ up to $z \sim 1.5$ and possibly beyond. While some individual sets of SNe Ia are now, by themselves, large enough to provide constraints on some cosmological parameters (Guy et al. 2010; Kessler et al. 2009), they do not yet constrain the properties of dark energy as well as the analyses that combine individual data sets to create a compilation of SNe Ia that covers a broader range of redshifts. In Kowalski et al. (2008), we developed a systematic methodology for combining the many available data sets into one compilation, called the "Union" compilation.

There are many positive features behind the philosophy adopted by the Union analysis. It includes all SN Ia data sets on an equal footing, with the same light-curve fitting, cuts, and outlier rejection. Estimates of the systematic error are entered into a covariance matrix, which can be used for fitting any cosmological model. Choices about how to perform the analysis and what cuts to apply are done with the cosmological results hidden. This type of "blind" analysis mitigates biases that arise from inadvertently scrutinizing some data more than others. In Amanullah et al. (2010), we adopted this strategy to create the Union2 compilation. This paper also revised and improved the Union analysis in several significant ways. First,

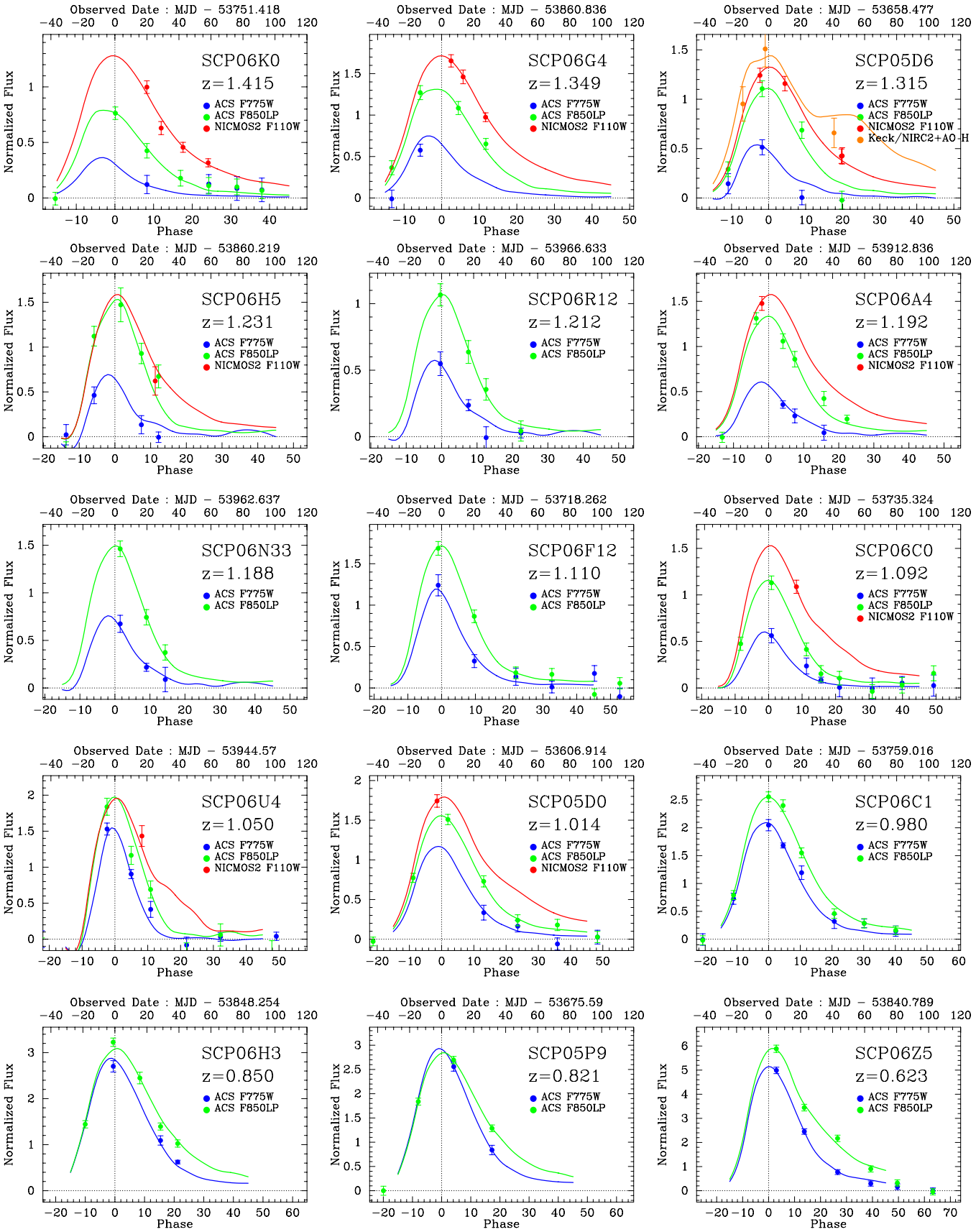

Figure 2. Fifteen SNe Ia light-curve fits by SALT2. Flux is normalized to the z_{850}-band zero-point magnitude. ACS i_{775}, ACS z_{850}, and NICMOS F110W data are color coded in blue, green, and red, respectively. Note that SCP 05D06 ($z = 1.314$) has H-band data from the Keck AO system (orange; Melbourne et al. 2007) and that these data are consistent with the *HST*/ACS and *HST*/NICMOS light-curve data.

it augmented the Union sample with new SN Ia data sets from the literature, including 102 low-redshift SNe Ia from the CfA3 survey (Hicken et al. 2009a), 129 intermediate-redshift SNe Ia from the Sloan Digital Sky Survey (SDSS) SN survey (Holtzman et al. 2008), 5 intermediate-redshift SNe Ia discovered from La Palma (Amanullah et al. 2008), and 6 new high-redshift SNe Ia. The paper revised the analysis by replacing the SALT light-curve fitter with SALT2 (Guy et al. 2005, 2007) and handled many systematic errors on an SN-by-SN basis in a covariance matrix.

In this paper, we use the analysis procedure that was used for the Union2 compilation with only one significant change: a correction for the host-mass-SN Ia–luminosity relation, described below. The *HST* calibration and the associated errors have also been updated, as described in Section 4.4.1. We refer to this new compilation as "Union2.1."

4.1. Host-mass Correction to SN Ia Luminosities

There is evidence that SN Ia luminosity correlates with the mass of the host galaxy, even after the corrections for color and light-curve width have been applied (Kelly et al. 2010; Sullivan et al. 2010; Lampeitl et al. 2010). Since low-redshift SNe Ia are predominantly from surveys that target cataloged galaxies, the host galaxies of SNe Ia in these surveys are, on average, more massive than the host galaxies of distant SNe Ia from untargeted surveys. SNe Ia from low-redshift samples therefore have brighter absolute magnitudes. Left uncorrected, the correlation biases cosmological results (Sullivan et al. 2010).

Sullivan et al. (2010) find that the correlation can be corrected by fitting a step in absolute magnitude at $m_\star^{\rm threshold} = 10^{10}\,m_\odot$. There are two complications with making this correction: most of the SNe in the Union2 compilation do not have host-mass data available in the literature and SN Ia hosts with masses close to the cutoff may scatter across, decreasing the fitted size of the step. To address these problems, we adopt a probabilistic approach to determining the proper host-mass correction to apply to each SN, correcting each SN by the probability that it belongs in the low-host-mass category. (The low-host-mass category was chosen because most of the low-redshift SNe are from high-mass galaxies, so correcting the low-host-mass SNe minimizes the correlation between M_B and the correction coefficient.)

Suppose we have a mass measurement $m_\star^{\rm obs}$ and we would like to estimate the probability that the true mass $m_\star^{\rm true}$ is less than the mass threshold. We begin by noting that

$$P\left(m_\star^{\rm obs}, m_\star^{\rm true}\right) = P\left(m_\star^{\rm obs}|m_\star^{\rm true}\right) P\left(m_\star^{\rm true}\right)\,. \quad (1)$$

We can then integrate this probability over all true host masses less than the threshold:

$$P\left(m_\star^{\rm true} < m_\star^{\rm threshold}|m_\star^{\rm obs}\right) = \int_{m_\star^{\rm true}=0}^{m_\star^{\rm threshold}} P\left(m_\star^{\rm obs}|m_\star^{\rm true}\right) P\left(m_\star^{\rm true}\right) \quad (2)$$

up to a normalization constant found by requiring the integral to be unity when integrating over all possible true masses. $P(m_\star^{\rm true})$ is estimated from the observed distribution for each type of survey. The Supernovae Legacy Survey (SNLS; Sullivan et al. 2010) and SDSS (Lampeitl et al. 2010) host masses were assumed to be representative of untargeted surveys, while the mass distribution in Kelly et al. (2010) was assumed to be typical of nearby targeted surveys. As these distributions are approximately log-normal, we use this model for $P(m_\star^{\rm true})$ using the mean and rms from the log of the host masses from these surveys (with the average measurement errors subtracted in quadrature), giving $\log_{10} P(m_\star^{\rm true}) = \mathcal{N}(\mu = 9.88, \sigma^2 = 0.92^2)$ for untargeted surveys and $\log_{10} P(m_\star^{\rm true}) = \mathcal{N}(10.75, 0.66^2)$ for targeted surveys. When host-mass measurements are available, $P(m_\star^{\rm obs}|m_\star^{\rm true})$ is also modeled as a log-normal; when no measurement is available, a flat distribution is used.

For an SN from an untargeted survey with no host-mass measurement (including SNe presented in this paper which are not in a cluster), $P(m_\star^{\rm true} < m_\star^{\rm threshold})$ is the integral of $P(m_\star^{\rm true})$ up to the threshold mass: 0.55. Similarly, nearby SNe from targeted surveys without host galaxy mass measurements are given a $P(m_\star^{\rm true} < m_\star^{\rm threshold})$ of 0.13. (Very similar numbers of 0.50 and 0.09 are derived from the observed distribution, without using the log-normal approximation.) We must make the correction for SNe in clusters, as these are from a targeted survey. We take advantage of the simpler SEDs of early-type galaxies to precisely measure these masses.[50]

The best-fit mass-correction coefficient, δ, is much smaller in magnitude (-0.03) than that found in other studies (≈ -0.08). This may be due to the small value for δ from the first-year SNLS data, as shown in Table 6. We include the difference in these two δs as a systematic, as discussed in Section 4.5. For this analysis, we assumed that the host-mass correction does not evolve with redshift.

4.2. Light-curve Fitting

In Amanullah et al. (2010), we use SALT2 (Guy et al. 2007) to fit SN light curves. The SALT2 model fits three parameters to each SN: an overall normalization, x_0, to the time-dependent SED of an SN Ia, the deviation, x_1, from the average light-curve shape, and the deviation, c, from the mean SN Ia $B-V$ color. The three parameters, x_1, c, and integrated B-band flux of the model SALT2 SED at maximum light, $m_B^{\rm max}$, are then combined with the host mass to form the distance modulus:

$$\mu_B = m_B^{\rm max} + \alpha\cdot x_1 - \beta\cdot c + \delta\cdot P\left(m_\star^{\rm true} < m_\star^{\rm threshold}\right) - M_B\,, \quad (3)$$

where M_B is the absolute B-band magnitude of an SN Ia with $x_1 = 0$, $c = 0$, and $P(m_\star^{\rm true} < m_\star^{\rm threshold}) = 0$. The parameters α, β, δ, and M_B are nuisance parameters that are fitted simultaneously with the cosmological parameters. The SN Ia photometry data and SALT2 light-curve fits are shown in Figure 2. The fitted SALT2 parameters are listed in Table 3 as well as the host galaxy host stellar mass and lensing magnification factor.

4.3. Union2.1

To the Union2 SN Ia compilation (Amanullah et al. 2010), we add 16 SNe Ia from this paper that were classified as either secure or probable, including 6 SNe Ia hosted by high-z cluster elliptical galaxies. The four SNe Ia that were classified as possible are not used. We also add 18 SNe Ia from the low-redshift sample of Contreras et al. (2010), 9 of which were not in Union2 (the others had published data from CfA). As in Union2, for all SNe we require

1. that the CMB-centric redshift is greater than 0.015;
2. that there is at least one point between -15 and 6 rest-frame days from B-band maximum light;

[50] C-001 and F-012 are in clusters, but are not hosted by early-type hosts. We use the untargeted value for their host-mass–luminosity relation correction.

Table 3
SALT2 Light-curve Fit Results

SN Name	z	$\mathrm{MJD}_{\mathrm{Bmax}}$	m_B	x_1	c	Galaxy Mass[a] ($10^{11}\ M_\odot$)	Lens Factor[b]
SCP06A4	1.192	53912.7 ± 1.5	25.497 ± 0.048	-1.45 ± 0.68	0.065 ± 0.084	0.44	...
SCP06C0	1.092	53735.4 ± 1.0	25.636 ± 0.066	-2.66 ± 0.65	0.257 ± 0.083	1.97	$1.030^{+0.007}_{-0.005}$
SCP06C1	0.980	53759.0 ± 0.7	24.613 ± 0.028	-0.35 ± 0.33	0.014 ± 0.053	...	...
SCP06F12	1.110	53718.4 ± 2.3	25.253 ± 0.068	-2.09 ± 1.29	-0.133 ± 0.142	...	...
SCP06G4	1.350	53860.9 ± 1.4	25.424 ± 0.052	0.15 ± 0.64	-0.029 ± 0.052	1.72	$1.015^{+0.005}_{-0.004}$
SCP06H3	0.850	53848.2 ± 0.6	24.345 ± 0.038	0.58 ± 0.31	0.089 ± 0.067	...	...
SCP06H5	1.231	53860.2 ± 1.5	25.389 ± 0.111	-3.12 ± 1.10	-0.103 ± 0.187	3.66	...
SCP06K0	1.415	53751.3 ± 2.8	25.811 ± 0.087	0.30 ± 0.97	0.147 ± 0.081	2.30	...
SCP06N33	1.188	53962.6 ± 4.3	25.407 ± 0.132	-2.15 ± 1.32	-0.038 ± 0.175	...	$1.066^{+0.017}_{-0.014}$
SCP05D0	1.014	53606.9 ± 0.9	25.201 ± 0.066	-0.61 ± 0.65	0.061 ± 0.085	0.40	...
SCP05D6	1.315	53658.5 ± 1.3	25.660 ± 0.046	-1.26 ± 0.56	-0.058 ± 0.061	2.61	$1.021^{+0.012}_{-0.008}$
SCP05P9	0.821	53675.6 ± 0.6	24.367 ± 0.049	0.25 ± 0.50	0.022 ± 0.075	...	...
SCP06R12	1.212	53966.6 ± 3.5	25.789 ± 0.114	-2.06 ± 1.50	-0.158 ± 0.198	0.23	...
SCP06U4[c]	1.050	53944.4 ± 1.1	25.056 ± 0.063	-4.62 ± 1.09	-0.102 ± 0.096	1.11	...
SCP06Z5	0.623	53840.5 ± 3.0	23.482 ± 0.144	-0.76 ± 0.88	0.070 ± 0.120	...	...

Notes.
[a] The details of host galaxy identifications, coordinates, and its stellar mass measurements can be found in Meyers et al. (2012).
[b] Gravitational lensing magnification factor (see Section 2.1 for details). For cosmological analysis we must divide the corrected SN fluxes by this factor to make use of these supernovae.
[c] SCP06U4 is not included in our current cosmological results, but will likely be included in future compilations (see Section 4 for details).

3. that there are at least five valid data points;
4. that the entire 68% confidence interval for x_1 lies between -5 and $+5$;
5. data from at least two bands with rest-frame central wavelength coverage between 2900 Å and 7000 Å; and
6. at least one band redder than rest-frame U band (4000 Å). This cut is new to this analysis, but only affects SN 2002fx, a GOODS SN that is very poorly measured.

In addition to these quality cuts, we removed any SN spectroscopically classified as SN 1991bg-like. These SNe Ia are a distinct subclass that is not modeled well by SALT2. In cases when spectroscopic sub-typing is not possible or not available, we screen for these SNe photometrically by searching for any SNe with red ($c > 0.2$) and narrow-width ($x_1 < -3$) light curves. In the current data set, none are cut by this screening. When fit with SALT2, and color-corrected and shape-corrected (as though they were normal SNe Ia), spectroscopically identified members of this class have an average absolute magnitude only 0.2 mag fainter than normal SNe Ia; any contamination from the handful of SNe near this cut will have only a small impact (and one well accounted for by our contamination systematic; see Amanullah et al. 2010).

From the 16 SNe Ia that were classified as either secure or probable (see Table 1), SN SCP06U4 and SN SCP06K18 fail to pass these cuts. SN SCP06K18 lacks good enough light-curve coverage and SN SCP06U4 fails the x_1 cut.[51] This leaves 14 SNe Ia that are used to constrain the cosmology.

4.4. Fitting the Cosmology

Following Amanullah et al. (2010), the best-fit cosmology is determined by minimizing

$$\chi^2_{\mathrm{stat}} = \sum_{\mathrm{SNe}} \frac{[\mu_B(\alpha, \beta, \delta, M_{\mathrm{B}}) - \mu(z; \Omega_m, \Omega_w, w)]^2}{\sigma^2_{\mathrm{lc}} + \sigma^2_{\mathrm{ext}} + \sigma^2_{\mathrm{sample}}}. \quad (4)$$

[51] Using an updated version (2-18-17) of SALT2 (or using SALT1), SN SCP06U4 would pass this cut, so this supernova may be included in future analyses.

A detailed discussion of the terms in this equation can be found in Amanullah et al. (2010). We only comment on the final term in the denominator, $\sigma^2_{\mathrm{sample}}$, which is computed by setting the reduced χ^2 of each sample to unity. This term was referred to as "$\sigma^2_{\mathrm{systematic}}$" in Kowalski et al. (2008) and Amanullah et al. (2010). We note that $\sigma^2_{\mathrm{sample}}$ includes intrinsic dispersion as well as sample-dependent effects. This term effectively further de-weights samples with poorer-quality data that has sources of error which have not been accounted for. As noted in Amanullah et al. (2010), this may occasionally deweight an otherwise well-measured SN.

Following Conley et al. (2006), Kowalski et al. (2008), and Amanullah et al. (2010), we hide our cosmology results until the full analysis approach is settled. As in previous Union analysis, we carry out an iterative χ^2 minimization with outlier rejection. Each sample is fit for a flat ΛCDM cosmology independently of the other samples (but with α, β, and δ set to their global values). An M_B is chosen for each sample by minimizing the absolute variance-weighted sum of deviations, minimizing the effects of outliers. We then reject any SN more than 3σ from this fit. All of the SNe Ia in our new sample pass the outlier rejection. As each sample is fit independently with its own Hubble line, systematic errors and the choice of cosmological model are not relevant in this selection.

4.4.1. Diagnostics

A diagnostic plot, which is used to study possible inconsistencies between SN Ia samples, is shown in Figure 3. The median of σ_{sample} can be used as a measure of the intrinsic dispersion associated with all SNe Ia. The intrinsic dispersion is a reflection of how well our empirical models correct for the observed dispersion in SN luminosities. The median σ_{sample} for this paper is 0.15 mag and is indicated with the leftmost dashed vertical line in the left panel.

The variance-weighted rms about the best-fit cosmology gives an indication of the quality of the photometry. A sample with more accurate photometry will have a smaller rms. For SNe Ia

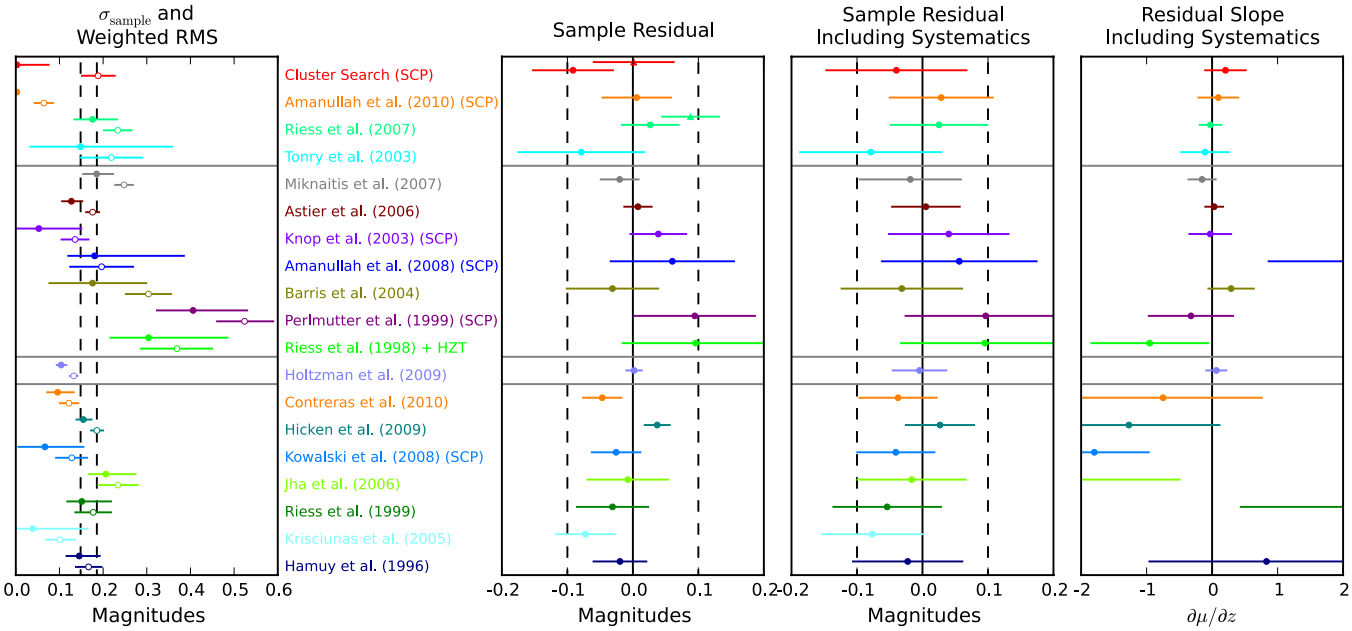

Figure 3. Diagnostics plot for the individual data sets. From left to right: irreducible sample dispersion (filled circles) and variance-weighted rms about the best-fit model (open circles); the average sample residual from the best-fit model ($\mu_{\rm measured} - \mu_{\rm model}$) excluding and including systematic errors; and the best-fit slope of the Hubble residual (in magnitudes) vs. redshift—$\partial\mu_{\rm residual}/\partial z$. Note that the errors on the sample dispersion include only statistical errors and do not include possible systematic errors. The confidence intervals on the weighed rms are obtained with Monte Carlo simulations. The triangles in the sample residual plot show the effect of including the filter shifts discussed in Section 4.4.1.

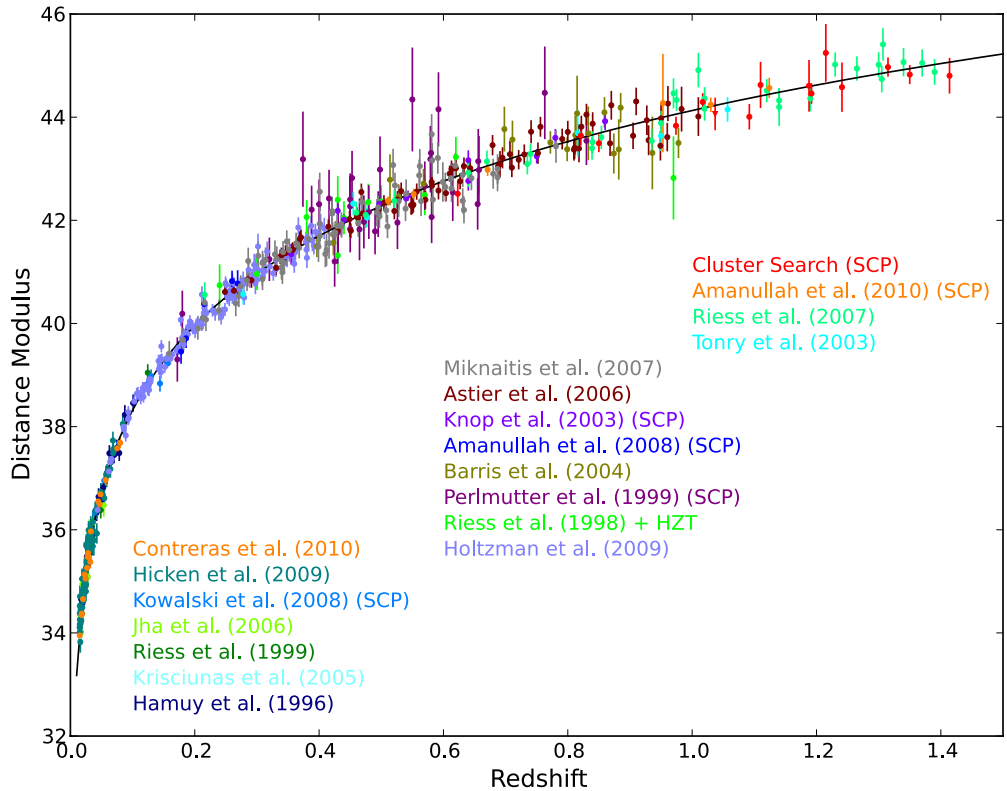

Figure 4. Hubble diagram for the Union2.1 compilation. The solid line represents the best-fit cosmology for a flat ΛCDM universe for supernovae alone. SN SCP06U4 falls outside the allowed x_1 range and is excluded from the current analysis. When fit with a newer version of SALT2, this supernova passes the cut and would be included, so we plot it on the Hubble diagram, but with a red triangle symbol.

from our survey, the rms is 0.19 ± 0.04, which is only slightly larger than that measured for the first-year SN Ia sample from SNLS, and equal to the median of all samples (shown as the rightmost dashed line in Figure 3, left panel).

The two middle panels show the tension between data sets, the first with statistical errors only and the second with statistical and systematic errors (see Section 4.5). Most samples land within 1σ of the mean defined by all samples and about one-third lie

outside 1σ, as expected for a normal distribution. No sample exceeds 2σ. The right panel shows the slope of the residuals, which, for larger data sets, can be used to reveal Malmquist-like biases or calibration errors.

The SNe from our sample are 1.5σ brighter than the average sample. While the source of the difference may certainly be a simple statistical fluctuation, part of the difference might be attributable to errors in the filter responses of the ACS filters. (The difference is largely driven by the SNe Ia that have only ACS i_{775} and z_{850} data to constrain their light curves.) Based on photometric observations of spectrophotometric standards, Bohlin (2007) reports possible blueward shifts of 94 Å for the z_{850} filter and 57 Å for the i_{775} filter (with smaller shifts in bluer filters). The red triangle in the sample residual panel shows the effect of applying these shifts. The shifts also affect the GOODS SNe. The green triangle shows the effect of applying the filter shifts to those data. Bohlin (2007) notes that more data to confirm the filter shifts are needed, so we do not apply them in our primary analysis. Instead, we include the uncertainty in the filter curves as a systematic error, as described in Section 4.5.

Part of the difference could also be due to the correction that we apply for the recently discovered correlation between host galaxy mass and the luminosity of SNe Ia after the light-curve width and color corrections have been applied. Many of the hosts in our sample are massive early-type galaxies. In this analysis, the correction we use is smaller than the correction that has been noted by others. We add this difference as a systematic error, as described in Section 4.5.

Figure 4 shows the Hubble Diagram with SNe from the updated Union2 sample and the best-fit ΛCDM model. We add 14 SNe Ia from this current paper. (As discussed above, SN SCP06U4 is likely to be included in future analyses so it is included on the plot with a different symbol.) Ten (11 with SN SCP06U4) are above a redshift of one, significantly increasing the number of well-measured SNe above this redshift.

4.5. Systematic Errors

In this paper, we follow the systematics analysis we presented in Amanullah et al. (2010). Systematic errors that directly affect SN distance measurements (calibration and galactic extinction, for example) are treated as nuisance parameters to be fit simultaneously with the cosmology. Minimizing over these nuisance parameters gives additional terms to add to the distance modulus covariance matrix:

$$U_{ij} = \sum_{\epsilon} \frac{d\mu_i(\alpha,\beta)}{d\epsilon} \frac{d\mu_j(\alpha,\beta)}{d\epsilon} \sigma_\epsilon^2 \,, \tag{5}$$

where the sum is over each of these distance systematic errors in the analysis. (Although the distance modulus depends on δ as well as α and β, the derivatives with respect to the zero points do not.) In this analysis, α and β have little interaction with cosmological parameters. When computing cosmological constraints, we therefore freeze the covariance matrix in order to avoid multiple matrix inversions.[52] Only when the α and β may vary significantly from the global best fit (Table 6) do we update α and β.

Systematic errors that affect sample composition or the color and shape correction coefficients cannot be parameterized SN by SN in this way. These are incorporated by assigning each data set its own constant covariance. This is an adequate treatment, as these systematic errors are subdominant.

There are two systematic errors that were not included in Amanullah et al. (2010) but are included in this analysis for the first time: a systematic error on the host-mass-correction coefficient, δ (which might affect δ at the ∼0.05 level), and uncertainties in the effective wavelengths of the ACS i_{775} and z_{850} filters.

In addition to updating the NICMOS F110W zero point and uncertainty, as described in Section 3.2.1, we revise the uncertainty assigned to the zero point for NICMOS F160W to account for the uncertainty in the count-rate nonlinearity at this wavelength (de Jong et al. 2006). Table 4 gives the assumed zero-point error for each filter.

We note that the nearby SNe from targeted searches are sensitive to δ (relative to the untargeted searches) at the level of $(0.55–0.13)\Delta\delta \approx 0.02$ mag, while the covariance-weighted mean of the cluster SNe varies with δ as $0.24\Delta\delta \approx 0.01$ mag. We cannot propagate this systematic on an SN-by-SN basis, as this would be equivalent to fitting for δ, which we already do. Therefore, we include this error by adding a covariance of 0.02^2 to the nearby targeted SN surveys, a covariance of 0.01^2 to our new data set, and 0.02×0.01 between these data sets.

Including uncertainties in filter effective wavelength is not as straightforward as including zero-point uncertainties. Effective wavelength is only the first-order method of describing a filter. For a simple filter shift, as implemented here, $d\mu(\alpha,\beta)/d\lambda$ will undergo significant variations as SN spectral features shift in and out of the filter. These are likely to be worse than the actual effect of simply reweighting filter throughput. Although in general these variations will be averaged out with different phases, redshifts, and additional filters, we have modeled a worst case in accounting for this systematic (and even then it only affects the SNe most dependent on z_{850}).

Table 5 shows the impact of each type of systematic error on our cosmological constraints, in combination with BAO, CMB, and H_0 data (see Section 5). For the purpose of constructing Table 5, for each systematic error in the table we add the contribution from just that systematic to the statistical-only covariance matrix. The confidence interval for constant w where the χ^2 is within 1 of the minimum χ^2 (the edges of this confidence interval are hereafter referred to with the notation $\Delta\chi^2 = 1$) is found iteratively; the plus and minus errors for constant w are averaged. The statistical-only constant w error bar is subtracted in quadrature, leaving the effect of each systematic on constant w. We also quote the effect of each systematic error of the $\Delta\chi^2 = 5.99$ confidence contour in the (w_0, w_a) plane; as this is two dimensional, we subtract the area (not in quadrature) of the statistical-only contour.

Since the derived cosmology errors vary with the best-fit cosmology, after a given systematic error has been added, the SN magnitudes are shifted so that the best-fit cosmology including that systematic matches the best fit with statistical errors only. This magnitude adjustment (which is the same adjustment we use for blinding ourselves to the best-fit cosmology) consists of repeatedly computing the difference in distance modulus between the best-fit cosmology and fiducial value and adding it to the SNe.

As with the Union2 compilation, calibration systematics represent the largest contribution to the error on constant w. Here, we see that they are also the dominant systematics for (w_0, w_a). As noted by Amanullah et al. (2010), significantly

[52] As demonstrated in the Union2 appendix, these matrix inversions can be simplified at the expense of more matrix multiplication; the run-time does not change much.

Table 4
Assumed Instrumental Uncertainties for SNe in This Paper

Source	Band	Uncertainty	Reference
HST	WFPC2	0.02	Heyer et al. (2004)
	ACS F850LP	0.01	Bohlin (2007)
	ACS F775W	0.01	
	ACS F606W	0.01	
	ACS F850LP	94 Å	Bohlin (2007)
	ACS F775W	57 Å	
	ACS F606W	27 Å	
	NICMOS J	0.024	P. Ripoche et al. (in preparation), Section 3.2.1
	NICMOS H	0.06	de Jong et al. (2006)
SNLS	*g*, *r*, *i*	0.01	Astier et al. (2006)
	z	0.03	
ESSENCE	*R*, *I*	0.014	Wood-Vasey et al. (2007)
SDSS	*u*	0.014	Kessler et al. (2009)
	g, *r*, *i*	0.009	
	z	0.010	
SCP: Amanullah et al. (2010)	*R*, *I*	0.03	Amanullah et al. (2010)
	J	0.02	
Other	*U*-band	0.04	Hicken et al. (2009a)
	Other band	0.02	Hicken et al. (2009a)

Table 5
Effect on Constant w Error Bars and Area of the 95% $w_0 - w_a$ Confidence Contour (Inverse DETF FoM) for Each Type of Systematic Error, When SN Ia Constraints are Combined with Constraints from CMB, H_0, and BAO

Source	Error on Constant w	Inverse DETF FoM
Vega	0.033	0.19
All instrument calibration	0.030	0.18
(ACS zero points)	0.003	0.01
(ACS filter shift)	0.007	0.04
(NICMOS zero points)	0.007	<0.01
Malmquist bias	0.020	0.07
Color correction	0.020	0.07
Mass correction	0.016	0.08
Contamination	0.016	0.05
Intergalactic extinction	0.013	0.03
Galactic extinction normalization	0.010	0.01
Rest-frame *U*-band calibration	0.009	<0.01
Light-curve shape	0.006	<0.01
Quadrature sum of errors/sum of area (not used)	*0.061*	*0.68*
Summed in covariance matrix	0.048	0.42

smaller systematic errors are derived by adding each covariance in the covariance matrix rather than adding the cosmological impacts together. This is due to the different redshift dependence of each systematic error, as well as some self-calibration that occurs as described in Amanullah et al. (2010).

Some potential systematic errors can be investigated by dividing the whole data set into subsets. Table 6 shows many of these divisions. All of the numbers are computed including SN systematics; the cosmological constraints are computed including BAO and CMB data. In short, we do not see any evidence of unknown systematic errors, requiring the cosmological impact to be smaller than the current errors.

The first subsets are subsets in redshift. These can be used to study possible evolution of correction coefficients for shape, color, and host mass. The redshift range 0.5–1 seems to show β and δ smaller in magnitude, but the revised SNLS sample (Guy et al. 2010) which uses a newer version of the calibration and light-curve fitting (as well as many more SNe) shows no signs of this. As we have already budgeted these systematic uncertainties, these updates will be within our error bars.

The next rows show the effect of changing δ from 0 to -0.08 (the size of the correction in Sullivan et al. 2010). Because a large error on δ is already included in the systematic error covariance matrix, this has less than a 0.01 effect on w, about 10 times smaller than it would have if we did not include this systematic.

Next, we consider systematics caused by potentially different populations of SNe. We perform a cut on the best-fit true x_1 or c of each SN (see Amanullah et al. 2010 for details). The cosmology in each case is compatible with the cosmology derived from the whole sample.

We now look at each of the four largest data sets for evidence of tension. The only tension found is in the first-year SNLS

Table 6
Constraints on Standardization and Cosmological Parameters for Subsets

Subset	Number	$M_B(h=0.7)$	α	β	δ	Ω_m	w
Whole Sample							
$z \geqslant 0.015$	580	$-19.321^{+0.030}_{-0.030}$	$0.121^{+0.007}_{-0.007}$	$2.47^{+0.06}_{-0.06}$	$-0.032^{+0.031}_{-0.031}$	$0.271^{+0.015}_{-0.014}$	$-1.013^{+0.068}_{-0.074}$
Correction Coefficients, Split by Redshift							
$0.015 \leqslant z \leqslant 0.10$	175	$-19.328^{+0.037}_{-0.038}$	$0.118^{+0.011}_{-0.011}$	$2.57^{+0.08}_{-0.08}$	$-0.027^{+0.054}_{-0.054}$	0.270 (fixed)	-1.000 (fixed)
$0.100 \leqslant z \leqslant 0.25$	75	$-19.371^{+0.054}_{-0.054}$	$0.146^{+0.019}_{-0.019}$	$2.56^{+0.18}_{-0.17}$	$-0.087^{+0.060}_{-0.060}$	0.270 (fixed)	-1.000 (fixed)
$0.250 \leqslant z \leqslant 0.50$	152	$-19.317^{+0.046}_{-0.046}$	$0.116^{+0.014}_{-0.013}$	$2.46^{+0.12}_{-0.12}$	$-0.042^{+0.066}_{-0.066}$	0.270 (fixed)	-1.000 (fixed)
$0.500 \leqslant z \leqslant 1.00$	137	$-19.307^{+0.048}_{-0.049}$	$0.124^{+0.019}_{-0.019}$	$1.46^{+0.19}_{-0.19}$	$0.023^{+0.060}_{-0.060}$	0.270 (fixed)	-1.000 (fixed)
$z \geqslant 1.000$	25	$-19.289^{+0.217}_{-0.254}$	$-0.019^{+0.072}_{-0.076}$	$3.48^{+1.13}_{-0.89}$	$-0.151^{+0.384}_{-0.446}$	0.270 (fixed)	-1.000 (fixed)
Effect of δ on w							
$z \geqslant 0.015$	580	$-19.340^{+0.026}_{-0.026}$	$0.123^{+0.007}_{-0.007}$	$2.47^{+0.06}_{-0.06}$	-0.080 (fixed)	$0.272^{+0.015}_{-0.014}$	$-1.004^{+0.067}_{-0.072}$
$z \geqslant 0.015$	580	$-19.303^{+0.031}_{-0.031}$	$0.120^{+0.007}_{-0.007}$	$2.47^{+0.06}_{-0.06}$	0.000 (fixed)	$0.271^{+0.015}_{-0.014}$	$-1.013^{+0.069}_{-0.075}$
Cosmological Results, Split by Light-curve Color and Shape							
$c \geqslant 0.05$	256	$-19.387^{+0.037}_{-0.038}$	$0.118^{+0.011}_{-0.011}$	$2.77^{+0.09}_{-0.09}$	$-0.057^{+0.052}_{-0.052}$	$0.269^{+0.015}_{-0.014}$	$-1.028^{+0.077}_{-0.084}$
$c \leqslant 0.05$	321	$-19.323^{+0.030}_{-0.030}$	$0.125^{+0.011}_{-0.010}$	$1.29^{+0.32}_{-0.33}$	$-0.057^{+0.038}_{-0.038}$	$0.275^{+0.015}_{-0.014}$	$-0.982^{+0.069}_{-0.075}$
$x_1 \geqslant -0.25$	311	$-19.366^{+0.041}_{-0.041}$	$0.020^{+0.026}_{-0.025}$	$2.58^{+0.10}_{-0.10}$	$-0.004^{+0.047}_{-0.047}$	$0.269^{+0.015}_{-0.014}$	$-1.037^{+0.077}_{-0.085}$
$x_1 \leqslant -0.25$	269	$-19.386^{+0.044}_{-0.045}$	$0.152^{+0.021}_{-0.020}$	$2.43^{+0.08}_{-0.08}$	$-0.087^{+0.050}_{-0.050}$	$0.267^{+0.015}_{-0.014}$	$-1.045^{+0.077}_{-0.084}$
Correction Coefficients and M_B for the Large Data Sets							
Hicken et al. (2009b)	94	$-19.314^{+0.055}_{-0.055}$	$0.115^{+0.015}_{-0.015}$	$2.74^{+0.11}_{-0.11}$	$-0.053^{+0.098}_{-0.099}$	0.270 (fixed)	-1.000 (fixed)
Holtzman et al. (2008)	129	$-19.336^{+0.051}_{-0.051}$	$0.149^{+0.014}_{-0.013}$	$2.40^{+0.15}_{-0.14}$	$-0.061^{+0.050}_{-0.050}$	0.270 (fixed)	-1.000 (fixed)
Miknaitis et al. (2007)	74	$-19.325^{+0.078}_{-0.080}$	$0.113^{+0.037}_{-0.035}$	$2.49^{+0.17}_{-0.16}$	0.000 (fixed)	0.270 (fixed)	-1.000 (fixed)
Astier et al. (2006)	71	$-19.292^{+0.047}_{-0.048}$	$0.145^{+0.019}_{-0.018}$	$1.70^{+0.18}_{-0.18}$	$-0.023^{+0.040}_{-0.040}$	0.270 (fixed)	-1.000 (fixed)
$z > 0.9$, Split by Galaxy Host							
Early type $z > 0.9$	13	$-19.388^{+0.139}_{-0.186}$	$0.112^{+0.139}_{-0.151}$	$3.16^{+1.84}_{-1.26}$	0.000 (fixed)	0.270 (fixed)	-1.000 (fixed)
Late type $z > 0.9$	15	$-19.141^{+0.067}_{-0.067}$	$0.094^{+0.049}_{-0.041}$	$0.49^{+0.85}_{-0.69}$	0.000 (fixed)	0.270 (fixed)	-1.000 (fixed)

Notes. M_B is the B-band corrected absolute magnitude; α, β, and δ are the light-curve shape, color, and host-mass-correction coefficients, respectively. The outlier rejection is redone each time, so the totals may not add up to the whole sample. The constraints are computed including BAO, CMB, and H_0 constraints and supernova systematic errors.

sample (Astier et al. 2006). Here, β and δ are both at odds with the whole sample, but as noted above, we do not believe this is a cause for concern.

The final two rows show the high-redshift sample split by host type; this is discussed in Section 6.2.

5. CONSTRAINTS ON DARK ENERGY

Following Amanullah et al. (2010), we constrain the properties of dark energy first using SNe Ia alone (with and without systematics), and then by combining the constraints derived from SNe Ia with those derived from the seven-year *Wilkinson Microwave Anisotropy Probe* data of the CMB (Komatsu et al. 2011), the position of the BAO peak from the combined analysis of the SDSS Data Release 7 and 2dFGRS data (Percival et al. 2010), and the measurement of the Hubble constant (H_0) from Cepheids (Riess et al. 2011).

The rate of expansion at redshift z, $H(z)$, is described by the Friedmann equation:

$$\frac{H^2(z)}{H_0^2} = \Omega_m(1+z)^3 + \Omega_k(1+z)^2 + \Omega_{\rm DE} \times \exp\left[\int 3(1+w(z))d\ln(1+z)\right], \quad (6)$$

where H_0 is the rate of expansion today, Ω_m and $\Omega_{\rm DE}$ are the matter and dark-energy density with respect to the critical density today, $w(z)$ is the dark-energy equation-of-state parameter, and $\Omega_k = 1 - \Omega_m - \Omega_{\rm DE}$ is the spatial curvature density of the universe. Distances, such as the luminosity distance, depend on the integral of $1/H(z)$ over redshift.

In this section, we consider the following models for dark energy:

1. ΛCDM—a cosmological constant in a flat universe.
2. wCDM—a constant equation-of-state parameter in a flat universe.
3. $o w$CDM—a constant equation-of-state parameter in a curved universe.
4. w_zCDM models—a time-varying equation-of-state parameter in universes with and without curvature.

The results for each of the models are listed in Table 7 and discussed in turn in the following subsections. Unless stated otherwise, the uncertainties represent the 68% confidence limits ($\Delta\chi^2 = 1$) and include both statistical uncertainties and systematic errors.

5.1. ΛCDM

In the ΛCDM model, the equation-of-state parameter is exactly -1 and does not vary with time. In a flat universe,

Table 7
Fit Results on Cosmological Parameters Ω_m, w_0, w_a, and Ω_k

Fit	Ω_m	Ω_m w/Sys	Ω_k	Ω_k w/Sys	w_0	w_0 w/Sys	w_a	w_a w/Sys
				ΛCDM				
BAO+CMB+H_0	$0.267^{+0.015}_{-0.014}$		0 (fixed)		-1 (fixed)		0 (fixed)	
SNe	$0.277^{+0.022}_{-0.021}$	$0.295^{+0.043}_{-0.040}$	0 (fixed)	0 (fixed)	-1 (fixed)	-1 (fixed)	0 (fixed)	0 (fixed)
SNe+BAO+H_0	$0.288^{+0.020}_{-0.019}$	$0.314^{+0.034}_{-0.031}$	0 (fixed)	0 (fixed)	-1 (fixed)	-1 (fixed)	0 (fixed)	0 (fixed)
SNe+CMB	$0.272^{+0.017}_{-0.017}$	$0.274^{+0.024}_{-0.022}$	0 (fixed)	0 (fixed)	-1 (fixed)	-1 (fixed)	0 (fixed)	0 (fixed)
SNe+CMB+H_0	$0.262^{+0.015}_{-0.014}$	$0.258^{+0.018}_{-0.017}$	0 (fixed)	0 (fixed)	-1 (fixed)	-1 (fixed)	0 (fixed)	0 (fixed)
SNe+BAO+CMB	$0.278^{+0.014}_{-0.013}$	$0.282^{+0.017}_{-0.016}$	0 (fixed)	0 (fixed)	-1 (fixed)	-1 (fixed)	0 (fixed)	0 (fixed)
SNe+BAO+CMB+H_0	$0.271^{+0.012}_{-0.012}$	$0.271^{+0.014}_{-0.014}$	0 (fixed)	0 (fixed)	-1 (fixed)	-1 (fixed)	0 (fixed)	0 (fixed)
				$o\Lambda$CDM				
BAO+CMB+H_0	$0.269^{+0.015}_{-0.014}$		$0.002^{+0.005}_{-0.005}$		-1 (fixed)		0 (fixed)	
SNe+CMB	$0.278^{+0.024}_{-0.023}$	$0.298^{+0.047}_{-0.044}$	$-0.002^{+0.009}_{-0.009}$	$-0.007^{+0.013}_{-0.014}$	-1 (fixed)	-1 (fixed)	0 (fixed)	0 (fixed)
SNe+CMB+H_0	$0.260^{+0.015}_{-0.015}$	$0.255^{+0.019}_{-0.017}$	$0.005^{+0.006}_{-0.006}$	$0.005^{+0.005}_{-0.006}$	-1 (fixed)	-1 (fixed)	0 (fixed)	0 (fixed)
SNe+BAO+CMB	$0.282^{+0.015}_{-0.014}$	$0.286^{+0.018}_{-0.017}$	$-0.004^{+0.006}_{-0.006}$	$-0.004^{+0.006}_{-0.007}$	-1 (fixed)	-1 (fixed)	0 (fixed)	0 (fixed)
SNe+BAO+CMB+H_0	$0.271^{+0.013}_{-0.012}$	$0.272^{+0.014}_{-0.014}$	$0.002^{+0.005}_{-0.005}$	$0.002^{+0.005}_{-0.005}$	-1 (fixed)	-1 (fixed)	0 (fixed)	0 (fixed)
				wCDM				
BAO+CMB+H_0	$0.263^{+0.016}_{-0.015}$		0 (fixed)		$-1.082^{+0.099}_{-0.112}$		0 (fixed)	
SNe	$0.281^{+0.067}_{-0.092}$	$0.296^{+0.102}_{-0.180}$	0 (fixed)	0 (fixed)	$-1.011^{+0.208}_{-0.231}$	$-1.001^{+0.348}_{-0.398}$	0 (fixed)	0 (fixed)
SNe+BAO+H_0	$0.309^{+0.029}_{-0.028}$	$0.320^{+0.035}_{-0.033}$	0 (fixed)	0 (fixed)	$-1.097^{+0.091}_{-0.106}$	$-1.076^{+0.117}_{-0.133}$	0 (fixed)	0 (fixed)
SNe+CMB	$0.271^{+0.018}_{-0.017}$	$0.279^{+0.025}_{-0.023}$	0 (fixed)	0 (fixed)	$-0.983^{+0.051}_{-0.056}$	$-0.955^{+0.075}_{-0.079}$	0 (fixed)	0 (fixed)
SNe+CMB+H_0	$0.262^{+0.016}_{-0.015}$	$0.259^{+0.018}_{-0.017}$	0 (fixed)	0 (fixed)	$-0.990^{+0.049}_{-0.054}$	$-1.003^{+0.064}_{-0.069}$	0 (fixed)	0 (fixed)
SNe+BAO+CMB	$0.278^{+0.014}_{-0.014}$	$0.285^{+0.018}_{-0.017}$	0 (fixed)	0 (fixed)	$-0.993^{+0.052}_{-0.055}$	$-0.951^{+0.075}_{-0.081}$	0 (fixed)	0 (fixed)
SNe+BAO+CMB+H_0	$0.272^{+0.013}_{-0.013}$	$0.271^{+0.014}_{-0.014}$	0 (fixed)	0 (fixed)	$-1.008^{+0.050}_{-0.054}$	$-1.013^{+0.068}_{-0.073}$	0 (fixed)	0 (fixed)
				owCDM				
BAO+CMB+H_0	$0.247^{+0.020}_{-0.018}$		$-0.013^{+0.009}_{-0.007}$		$-1.391^{+0.252}_{-0.252}$		0 (fixed)	
SNe+CMB	$0.281^{+0.069}_{-0.087}$	$0.295^{+0.109}_{-0.161}$	$-0.003^{+0.034}_{-0.027}$	$-0.005^{+0.067}_{-0.041}$	$-1.007^{+0.179}_{-0.194}$	$-0.993^{+0.299}_{-0.331}$	0 (fixed)	0 (fixed)
SNe+CMB+H_0	$0.249^{+0.020}_{-0.018}$	$0.248^{+0.020}_{-0.018}$	$0.010^{+0.008}_{-0.008}$	$0.013^{+0.011}_{-0.010}$	$-0.937^{+0.063}_{-0.070}$	$-0.893^{+0.100}_{-0.109}$	0 (fixed)	0 (fixed)
SNe+BAO+CMB	$0.283^{+0.016}_{-0.015}$	$0.287^{+0.018}_{-0.017}$	$-0.004^{+0.007}_{-0.007}$	$-0.002^{+0.008}_{-0.008}$	$-1.012^{+0.058}_{-0.062}$	$-0.975^{+0.094}_{-0.098}$	0 (fixed)	0 (fixed)
SNe+BAO+CMB+H_0	$0.272^{+0.013}_{-0.013}$	$0.272^{+0.015}_{-0.014}$	$0.002^{+0.006}_{-0.006}$	$0.002^{+0.007}_{-0.007}$	$-1.006^{+0.056}_{-0.060}$	$-1.003^{+0.091}_{-0.095}$	0 (fixed)	0 (fixed)
				w_zCDM				
SNe+CMB	$0.273^{+0.022}_{-0.020}$	$0.281^{+0.043}_{-0.028}$	0 (fixed)	0 (fixed)	$-1.006^{+0.165}_{-0.182}$	$-0.993^{+0.263}_{-0.307}$	$0.11^{+0.75}_{-0.77}$	$0.17^{+1.08}_{-1.19}$
SNe+CMB+H_0	$0.259^{+0.017}_{-0.016}$	$0.256^{+0.019}_{-0.017}$	0 (fixed)	0 (fixed)	$-0.928^{+0.142}_{-0.143}$	$-0.880^{+0.222}_{-0.222}$	$-0.29^{+0.60}_{-0.66}$	$-0.52^{+0.86}_{-0.98}$
SNe+BAO+CMB	$0.278^{+0.014}_{-0.014}$	$0.284^{+0.018}_{-0.017}$	0 (fixed)	0 (fixed)	$-1.052^{+0.126}_{-0.120}$	$-1.013^{+0.183}_{-0.173}$	$0.30^{+0.48}_{-0.62}$	$0.26^{+0.57}_{-0.74}$
SNe+BAO+CMB+H_0	$0.271^{+0.013}_{-0.013}$	$0.270^{+0.015}_{-0.014}$	0 (fixed)	0 (fixed)	$-1.021^{+0.123}_{-0.117}$	$-1.046^{+0.179}_{-0.170}$	$0.07^{+0.49}_{-0.60}$	$0.14^{+0.60}_{-0.76}$
				ow_zCDM				
SNe+CMB	$0.177^{+0.086}_{-0.093}$	$0.190^{+0.208}_{-0.154}$	$0.075^{+0.065}_{-0.128}$	$0.073^{+0.115}_{-0.141}$	$-0.988^{+0.176}_{-0.202}$	$-0.969^{+0.284}_{-0.345}$	$0.90^{+0.26}_{-3.88}$	$0.89^{+0.43}_{-5.25}$
SNe+CMB+H_0	$0.247^{+0.020}_{-0.018}$	$0.255^{+0.026}_{-0.024}$	$0.014^{+0.026}_{-0.012}$	$0.036^{+0.016}_{-0.032}$	$-0.998^{+0.158}_{-0.224}$	$-1.106^{+0.355}_{-0.149}$	$0.36^{+0.85}_{-0.86}$	$1.05^{+0.20}_{-1.75}$
SNe+BAO+CMB	$0.283^{+0.019}_{-0.017}$	$0.286^{+0.022}_{-0.023}$	$-0.004^{+0.017}_{-0.010}$	$-0.001^{+0.037}_{-0.013}$	$-1.010^{+0.169}_{-0.178}$	$-0.997^{+0.266}_{-0.293}$	$-0.01^{+1.04}_{-1.05}$	$0.13^{+1.16}_{-1.57}$
SNe+BAO+CMB+H_0	$0.270^{+0.014}_{-0.013}$	$0.274^{+0.016}_{-0.015}$	$0.025^{+0.008}_{-0.008}$	$0.027^{+0.012}_{-0.011}$	$-1.218^{+0.069}_{-0.072}$	$-1.198^{+0.100}_{-0.112}$	$1.21^{+0.10}_{-1.14}$	$1.19^{+0.13}_{-0.13}$
SNe+BAO+CMB+H_0[a]	$0.270^{+0.029}_{-0.026}$	$0.274^{+0.032}_{-0.029}$	$0.025^{+0.016}_{-0.035}$	$0.027^{+0.026}_{-0.036}$	$-1.218^{+0.425}_{-0.147}$	$-1.198^{+0.293}_{-0.227}$	$1.21^{+0.19}_{-2.49}$	$1.19^{+0.27}_{-2.40}$

Notes. The parameter values are followed by their statistical (first column) and statistical and systematic (second column) 1σ ($\Delta\chi^2 = 1$) uncertainties. For the fits including curvature and time-varying w, the confidence intervals can be quite non-Gaussian and we also show $\Delta\chi^2 = 4$ confidence intervals (with and without systematics) for comparison.
[a] $\Delta\chi^2 = 4.0$.

SNe Ia alone constrain the dark-energy density, Ω_Λ, to be $\Omega_\Lambda = 0.705^{+0.040}_{-0.043}$. In Figure 5, we show the confidence intervals on Ω_m and Ω_Λ from SNe, CMB, and BAO. Both the individual constraints and the combined constraint are shown (the BAO constraints are computed with an $\Omega_m h^2$ prior from the CMB). The SN constraint is almost orthogonal to that of the CMB. Adding the constraints from CMB, BAO, and H_0 reduces the uncertainty. Under the assumption of a flat universe, the four probes yield

$$\Omega_\Lambda = 0.729^{+0.014}_{-0.014} \quad (\Lambda\mathrm{CDM} : \mathrm{SN} + \mathrm{CMB} + \mathrm{BAO} + H_0).$$

In this ΛCDM model, the expansion of the universe switched from deceleration to acceleration at $z = 0.752 \pm 0.041$, which

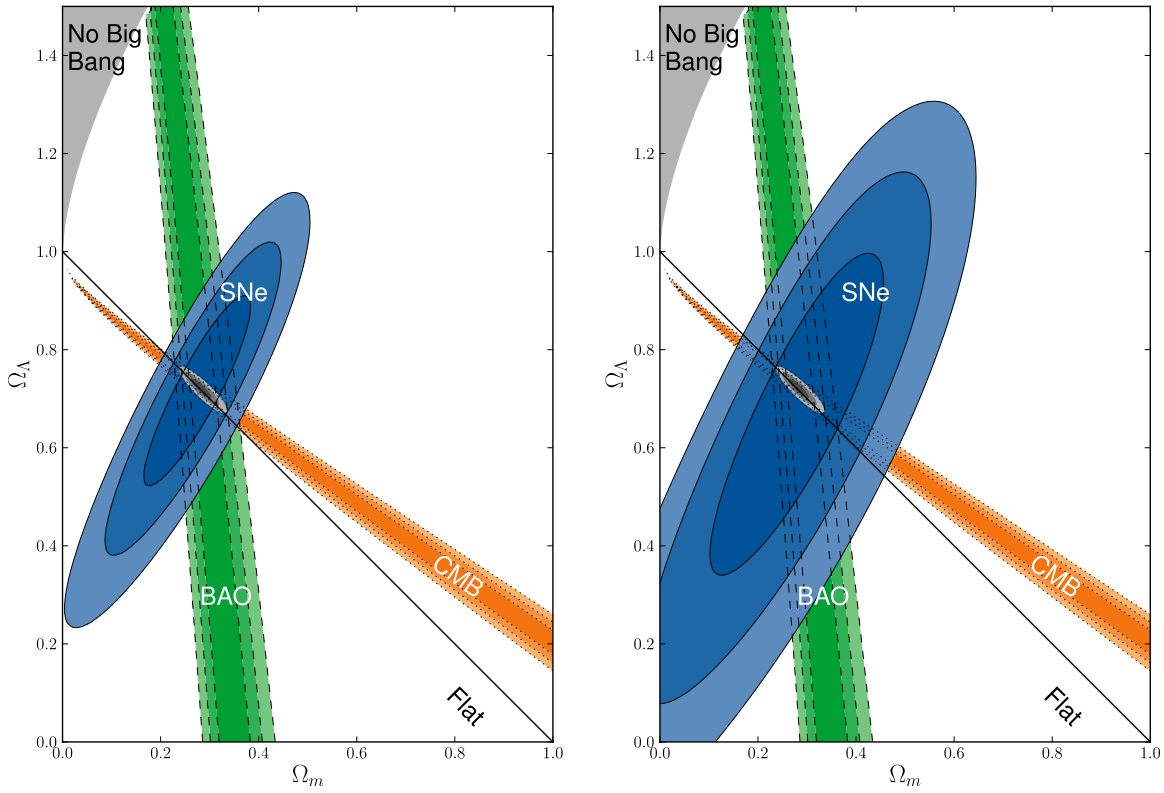

Figure 5. ΛCDM model: 68.3%, 95.4%, and 99.7% confidence regions of the $(\Omega_m, \Omega_\Lambda)$ plane from SNe Ia combined with the constraints from BAO and CMB. The left panel shows the SN Ia confidence region only including statistical errors, while the right panel shows the SN Ia confidence region with both statistical and systematic errors.

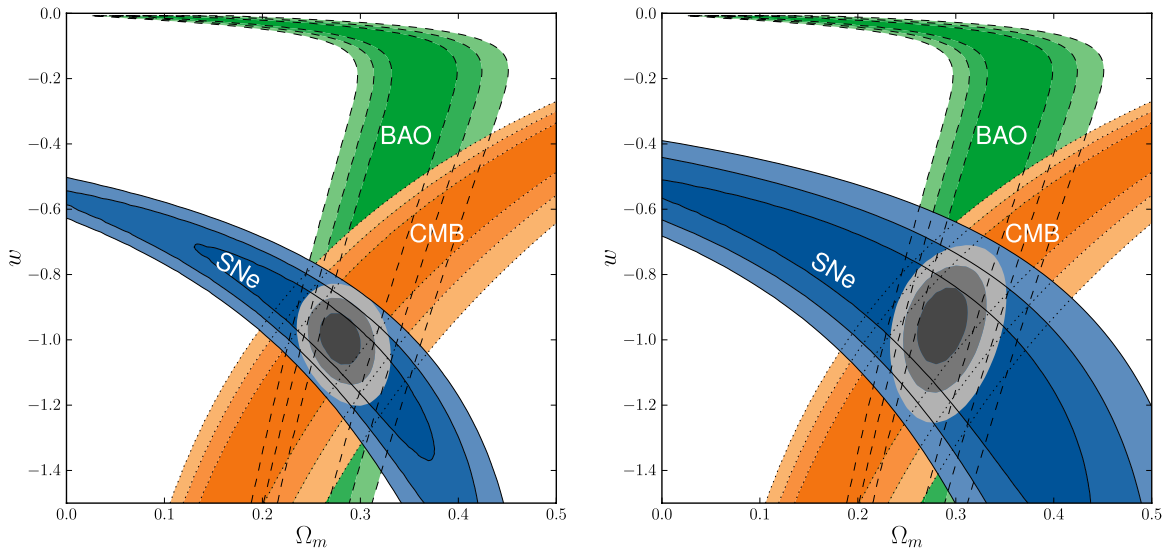

Figure 6. wCDM model: 68.3%, 95.4%, and 99.7% confidence regions in the (Ω_m, w) plane from SNe Ia, BAO, and CMB are shown in both panels. The left panel shows the SN Ia confidence region for statistical uncertainties only, while the right panel shows the confidence region including both statistical and systematic uncertainties. We note that CMB and SN Ia constraints are orthogonal, making this combination of cosmological probes very powerful for investigating the nature of dark energy.

corresponds to a look-back time of 6.62 ± 0.22 Gyr, about the half of the age of the universe. Equality between the energy density of dark energy and matter occurred later, at $z = 0.391 \pm 0.033$ or a look-back time of 4.21 ± 0.27 Gyr.

If we remove the flatness prior (labeled as $o\Lambda$CDM in Table 7), the best-fit Ω_m and Ω_Λ change by a fraction of their errors with $\Omega_k = 0.002^{+0.005}_{-0.005}$.

5.2. *wCDM: Constant Equation-of-state Parameter*

In wCDM models, w is constant but is allowed to be different from -1. While few dark-energy theories give $w \neq -1$ and yet constant (Copeland et al. 2006), constraints on the constant w model are still useful. The wCDM model contains fewer parameters than the dynamical dark-energy models considered in the following section, yet a value different from $w = -1$

would still provide insights for alternative theories for dark energy.

In a flat universe ($\Omega_k = 0$), SNe Ia alone give $w = -1.001^{+0.348}_{-0.398}$. Adding the constraints from the other three probes tightens the constraint on w considerably, as the constraints from SNe Ia in the $\Omega_m - w$ parameter plane are almost orthogonal to those provided by BAO and the CMB (Figure 6).

In principle, a constraint on H_0 helps to break the degeneracy between Ω_m and h for CMB, which measures $\Omega_m h^2$ (Spergel et al. 2003). However, in this case adding SN data helps more, as narrowing the degeneracy between Ω_m and w allows the CMB itself to constrain H_0. By combining all four probes, we find $w = -1.013^{+0.068}_{-0.073}$. As seen in Table 7, neither BAO nor H_0 currently make much of a difference in the error bars for this model.

5.3. owCDM: Constant Equation of State in a Curved Universe

Inflation models generally predict that the curvature of the universe, Ω_k, is $\sim 10^{-5}$ (Guth 1981; Liddle & Lyth 2000). In curved universes, SNe Ia play the critical role in constraining w, while CMB+BAO constrain Ω_k and Ω_m. By combining all four probes, we find $\Omega_k = 0.002^{+0.007}_{-0.007}$ and $w = -1.003^{+0.091}_{-0.095}$. Even with the additional freedom for non-zero curvature, a flat universe is supported from observations. Among many cosmological parameters, the curvature of the universe is the most well-determined parameter.

We note that CMB alone does not place a tight constraint on curvature,[53] $\Omega_k = -0.102^{+0.085}_{-0.097}$ (Komatsu et al. 2011). In order to break the degeneracy between Ω_m, Ω_k, and H_0 that exists in the CMB constraints, we need to add constraints either from BAO or H_0; this reduces the curvature uncertainty by a factor of 10. However, the combination of these three probes does not place a tight constraint on the equation-of-state parameter w. SNe improve the constraint on w from CMB+BAO+H_0 by more than a factor of three.

5.4. Time-dependent Equation of State

We next examine models in which dark energy changes with time. For a wide range of dark-energy models, it can be shown (Linder 2003) that, to good approximation, the dark-energy equation of state can be parameterized by

$$w(a) = w_0 + w_a(1 - a), \tag{7}$$

where $a = 1/(1 + z)$ is a scale factor. The ΛCDM model is recovered when $w_0 = -1$ and $w_a = 0$. The constraints on w_0 and w_a are shown in Figure 7 and Table 7.

The Dark Energy Task Force (Albrecht et al. 2006) proposed a figure of merit (FoM) for cosmological measurements equal to the inverse of the area of the 95% confidence contour in the $w_0 - w_a$ plane. When we make this measurement, using the $\Delta\chi^2 = 5.99$ contour, we find an FoM of 1.84 (statistical-only) and 1.04 (including systematics). Frequently, the FoM is also defined in terms of the 1σ errors ($\Delta\chi^2 = 1$); this FoM is 39.3 (statistical-only) and 22.6 (including systematics). Surprisingly, even with w_a floating, we still find an interesting constraint on Ω_k of ~ 0.02.

We next consider a model in which the dark-energy equation-of-state parameter is constant inside fixed redshift bins. This model has more parameters (and thus more freedom) than $w_0 - w_a$. The results are shown in Figure 8 and Table 7. We adopt the redshift bins used in Amanullah et al. (2010) so that a direct comparison can be made.

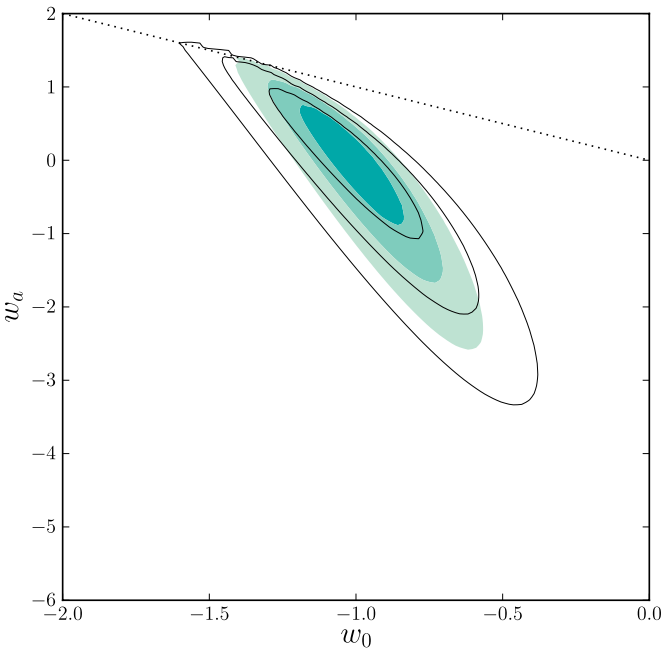

Figure 7. 68.3%, 95.4%, and 99.7% confidence regions of the (w_0, w_a) plane from SNe combined with the constraints from BAO, CMB, and H_0, both with (solid contours) and without (shaded contours) systematic errors. Zero curvature has been assumed. Points above the dotted line ($w_0 + w_a > 0$) violate early matter domination and are disfavored by the data.

(A color version of this figure is available in the online journal.)

In the left panel with broad bins, we show a reasonably good measurement of the equation-of-state parameter from redshift 0 to 0.5. From redshift 0.5 to 1, there is no real constraint. For example, any scalar field model ($|w| < 1$) is reasonably compatible with the data. Above redshift 1, the constraints are weaker. $w \gtrsim 0$ is ruled out, as this violates early matter domination.

We separate the SN and early universe constraints by defining a bin at redshift 1.6, as shown in the middle panel. This shifts the confidence interval for $w(1.0 < z < 1.6)$ toward higher w. Eliminating this division, and instead adding more bins up to redshift 0.5 (right panel), gives three constraints of moderate quality with a possible crossing of $w = -1$. No matter the binning, we will need more data extending above redshift 1 to investigate the dark-energy equation-of-state parameter where the uncertainty is still very large.

To examine constraints on the existence of dark energy at different epochs, we study $\rho(z)$, which is the density of the dark energy and is allowed to have different values in fixed redshift bins. Within each bin, ρ is constant. (Note that the discontinuities in $\rho(z)$ at the bin boundaries introduce discontinuities in $H(z)$.) We choose the same binning as above, but note that binned ρ and binned w models give different expansion histories. Our results are shown in Figure 9 and Table 8.

Although there is no real constraint on the equation-of-state parameter at redshift 0.5–1, dark energy is seen at high significance in both panels. There is weak evidence for the existence of dark energy above redshift 1, as can be seen in the left panel. However, if we again separate the SN data and early universe constraints (right panel) we see neither probe has any constraint on the existence of dark energy above redshift 1.

[53] http://lambda.gsfc.nasa.gov/product/map/dr4/parameters.cfm

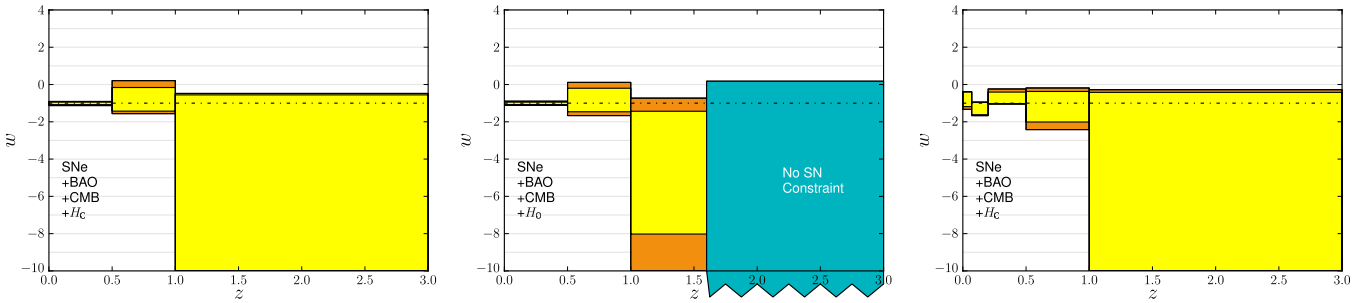

Figure 8. Constraints on $w(z)$, where $w(z)$ is assumed to be constant in each redshift bin, are plotted at the 68% probability level ($\Delta\chi^2 = 1$). Each panel shows different redshift binning. The results were obtained assuming a flat universe for the joint data set of SNe, BAO, CMB, and H_0, with (dark/orange) and without (light/yellow) SN systematics. The middle panel takes a closer look at the $z > 1$ constraints, while the right panel shows the effects of w binning at low redshift. In this panel the best-fit values of w cross $w = -1$ twice at low redshift, an unusual feature in dark-energy models. We note that the ΛCDM model is consistent with our $w(z)$ constraints for each of these binnings.

(A color version of this figure is available in the online journal.)

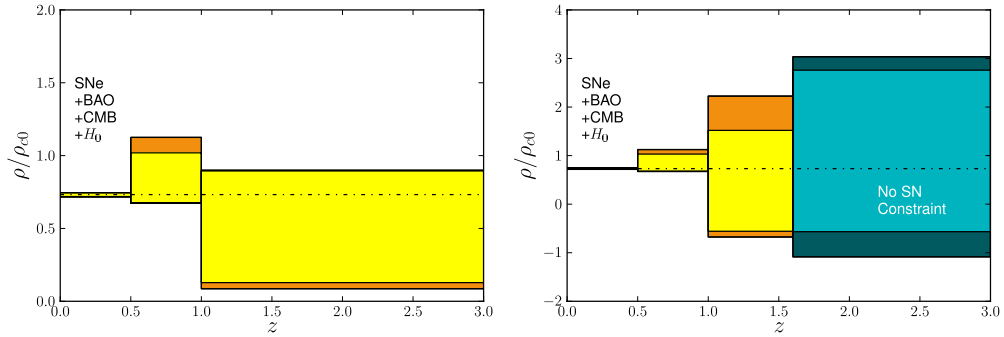

Figure 9. Redshift evolution of dark-energy density: constraints on $\rho(z)$ are shown as a function of redshift, where $\rho(z)$ is the density of the dark energy at a given redshift bin and is assumed to be constant within the redshift bin. $\rho(z)$ is normalized by the critical density today (ρ_{c0}) and is plotted at the 68% probability level ($\Delta\chi^2 = 1$). The results were obtained assuming a flat universe for the joint data set of SNe Ia, BAO, CMB, and H_0, with (dark/orange) and without (light/yellow) SN systematics. The two panels demonstrate different redshifts binning and have different scales.

(A color version of this figure is available in the online journal.)

Table 8
Constraints on Redshift Binned Equation-of-state w and Density ρ (Normalized by the Current Critical Density)

		$z < 0.5$	$0.5 < z < 1.0$	$1.0 < z < 1.6$	$z > 1.6$ [a]
$w(z)$	Stat Only:	$-1.013^{+0.067}_{-0.069}$	$-0.78^{+0.58}_{-0.68}$	$-3.7^{+2.2}_{-4.4}$	<0.18
	w/Sys:	$-1.006^{+0.110}_{-0.113}$	$-0.69^{+0.80}_{-0.98}$	$-3.9^{+3.2}_{-8.2}$	<0.24
$\rho_{DE}(z)/\rho_{c0}$	Stat Only:	$0.732^{+0.013}_{-0.014}$	$0.85^{+0.18}_{-0.17}$	$0.23^{+1.29}_{-0.79}$	$0.9^{+1.9}_{-1.5}$
	w/Sys:	$0.731^{+0.014}_{-0.015}$	$0.88^{+0.24}_{-0.21}$	$0.33^{+1.90}_{-1.00}$	$0.7^{+2.4}_{-1.8}$

Notes. Constraints on binned $\rho_{DE}(z)/\rho_{c0}$ and $w(z)$. This redshift binning corresponds to the middle panel of Figure 8 and the right panel of Figure 9. The constraints are computed including SNe, BAO, H_0, and CMB data.

[a] We note that the weak constraints in these bins come mostly from the CMB (which tells us that the early universe was matter dominated) and are only indirectly constrained by supernovae.

6. DISCUSSION

6.1. Improving the Constraints on Time-varying w by Efficiently Adding z > 1 SNe

Beyond $z = 1$, we add 10 new well-measured SNe Ia to the Hubble diagram. The variance-weighted rms scatter of the new sample is 0.20 ± 0.05 mag. As a comparison, the 15 $z > 1$ SNe Ia from the GOODS survey that pass our Union2 selection cuts have a variance-weighted rms scatter of 0.25 ± 0.05 mag. The new sample almost doubles the weight of *HST*-discovered SNe Ia beyond $z = 1$. The increase provides improvements on the most difficult-to-measure parameters, those that describe the time-varying properties of dark energy: $\rho(z)$ and $w(z)$ at the higher redshifts. In particular, the SNe from this search improve the constraint on $\rho(z)$ at redshifts $1.0 < z < 1.6$ by 28% (statistical errors only) and 18% (including SN systematics) after adding the constraints from the CMB, BAO, and H_0 (using the binning illustrated in the right panel of Figure 9). (It is more difficult to compare binned w results, as the constraints are much less Gaussian and more sensitive to the location of the best fit.)

The new sample is also obtained with greater observing efficiency with *HST*. Considering the number of $z > 1$ SNe Ia that satisfy the Union2 selection cuts, the yield of SNe Ia increases from a rate of one SN Ia per 43 *HST* orbits in the GOODS survey to one SN Ia per 22 *HST* orbits in this survey.

6.2. Splitting the Sample According to Host Galaxy Type

SNe Ia are well standardized with a small dispersion in magnitudes across the whole class. Any clues to heterogeneous characteristics therefore offer exciting possibilities to *further* improve standardization, enhancing the use of SNe as a cosmological probe. There is now evidence from studies of large samples of SNe Ia at both low and intermediate redshifts ($0 < z \lesssim 0.8$) that SN Ia properties are related to the properties of the host. The clearest of these is the relation between light-curve width and the specific star formation rate. SNe Ia in passive galaxies tend to have narrower light curves than SNe Ia that are in galaxies that are actively forming stars.

More than two-thirds of our new SNe Ia beyond $z = 0.9$ are hosted by early-type galaxies (Meyers et al. 2012). In field surveys, such as the GOODS survey, this ratio is inverted. By combining SNe Ia from our *HST* Cluster SN Survey and GOODS, together with our $z > 0.9$ SNe Ia in Amanullah et al. (2010), which have *HST* images of the host, we can create a sample of SNe Ia that has roughly equal numbers when split according to host type. When split this way, we find that $z > 1$ SNe Ia in early galaxies rise and fall more quickly than SNe Ia in later host types, thus extending the redshift interval over which the effect is now detected. Finding that low- and high-redshift SNe Ia follow similar trends gives us confidence that we can use very distant events to constrain cosmological parameters. This finding is reported in more detail in Meyers et al. (2012).

There is also evidence from SNe Ia at low and intermediate redshifts for other correlations with host type. Sullivan et al. (2010) find that both β and the rms scatter about the Hubble diagram are smallest for SNe Ia in passive galaxies. These trends suggest that dust plays a greater role in reddening and dimming SNe Ia in late-type galaxies. We examined our $z > 0.9$ sample for evidence of similar correlations using our host classification from Tables 3 and 4 of Meyers et al. (2012).

After correcting SN Ia luminosities for light-curve shape, SN Ia color and host galaxy mass (with the global values of these correction coefficients), we measure a sample dispersion of $0.14^{+0.11}_{-0.08}$ mag for SNe Ia in early-type galaxies and $0.14^{+0.06}_{-0.05}$ mag for SNe Ia in late-type galaxies. In terms of the rms, we find 0.23 ± 0.05 mag and 0.26 ± 0.05 mag for early- and late-type samples, respectively. The uncertainties are currently too large to distinguish between the two samples. Similarly for β, the errors are larger than the difference between the two samples, as seen in Table 6. Clearly, higher quality data of a larger number of $z > 0.9$ SNe Ia in both early- and late-type galaxies are required before the trends that are seen at low redshift can be detected in high-redshift samples.

We also examined the error-weighted difference in the brightness of SNe Ia in the two samples after correcting for light-curve shape and color, but without correcting for the host-mass–luminosity relation (setting $\delta = 0$) and find that SNe Ia in early-type galaxies are 0.18 ± 0.09 mag brighter. Since early-type galaxies are typically more massive than late-type galaxies, this 2σ difference, if confirmed with larger statistics, may be related to host galaxy mass.

6.3. Future Directions with Current Instrumentation

Due to the much improved sensitivity of the WFC3 IR detector, it will be feasible to measure $z > 1$ SNe with much better precision. The color measurement errors ($\sim$0.03 in $B - V$) can be made comparable to the color measurement errors in the SDSS SN survey (Smith et al. 2002; Holtzman et al. 2008). Assuming that the intrinsic dispersion of SN Ia luminosities does not change with redshift, the variance-weighted rms of the WFC3 sample should be similar to that measured for the SDSS, i.e., $\sim$0.14 mag. A well-observed SN Ia with WFC3 should have a statistical weight of two to three SNe Ia from the Cluster and GOODS surveys.

With a sufficient number of well-measured $z > 1$ SNe Ia with WFC3, it should be possible to search for the correlations between the properties of SNe Ia and their hosts that are seen at lower redshifts. As discussed above, current samples at $z > 1$ are too small to detect most of these differences. With the improved WFC3 photometry, only 40 SNe Ia, split evenly between early- and late-type hosts, would be needed to constrain a difference in β to an uncertainty of 0.4, which is about half the difference found for lower redshift SNe Ia (Sullivan et al. 2010). These samples would be just enough to see evidence of the lower rms for passive hosts seen by Sullivan et al. (2010).

Current WFC3 SN Ia surveys target empty fields, which means that there will be few SNe Ia in passive host galaxies. A WFC3 SN Ia survey that spends part of its time targeting $z \gtrsim 1$ clusters would ensure a better balance between host types while increasing the overall yield.

In order to investigate the FoM constraints possible with WFC3, we simulate a sample of 40 SNe at redshift 1.2 and add this sample into the current compilation. As there is a hard wall at $w_0 + w_a = 0$ when including BAO and CMB data, we simply fix Ω_m, rather than including BAO and CMB data (the alternative would be to adjust the SN magnitudes to a cosmology model far away from the wall). When adding these SNe, the statistical FoM improves by 39%. By the same metric, the current cluster sample improves the FoM by 10%.

6.4. Reducing the Systematic Errors for Future Surveys

As has been stressed by several authors, systematic errors are now larger than statistical errors. To fully utilize the potential of current and future SN Ia surveys to constrain cosmology, it will be necessary to reduce these errors significantly.

The largest current source of systematic uncertainty is calibration. Calibration uncertainties can be split into uncertainties related to the primary standard and uncertainties in instrumental zero points and bandpasses. In principle, all of these uncertainties can be reduced by establishing a network of well-calibrated standard stars and monitoring telescope system throughputs (Regnault et al. 2009). The SDSS demonstrated that a 1% relative photometric calibration is possible with the current standard star network and system throughput monitoring (Doi et al. 2010).

The ongoing Nearby Supernova Factory (SNf) project (Aldering et al. 2002) is aiming to provide the network of standard stars. SNf will also address the systematic uncertainty due to host-mass correction since the range of host masses would become comparable to that of high redshift for the first time. Additionally, the comprehensive SN Ia spectral time series from the SNf will allow one to tackle systematic uncertainties related to modeling of the light curves.

In the future, recently approved experiments such as Absolute Color Calibration Experiment for Standard Stars (Kaiser et al. 2010) and the proposed National Institute for Standards and Technology STARS project (McGraw et al. 2010; Zimmer et al. 2010) are aiming to achieve sub-percent absolute flux calibration for the network of stars in the wavelength range of visible to NIR. With this network of stars and with new techniques for monitoring throughput of the telescopes (Stubbs et al. 2007), we

will be able to cross-calibrate systems and reduce the systematic errors below the statistical errors.

7. SUMMARY AND CONCLUSIONS

We present *HST*/ACS, *HST*/NICMOS, and Keck AO-assisted photometry of 20 SNe Ia in the redshift range $0.63 < z < 1.42$. The SNe Ia were discovered in the *HST* Cluster Supernova Survey, a survey run by the Supernova Cosmology Project to search for SNe Ia in fields centered on 25 distant galaxy clusters (Dawson et al. 2009).

We implement new techniques to improve the accuracy of *HST* photometry. In particular, for data taken with NICMOS, which samples the rest-frame *B* and *V* bands of $z > 1$ SNe Ia, we use a more direct, more accurate measure of the NICMOS zero point (Ripoche et al. 2012), and we remove the residual background that persists after standard processing of NICMOS data with the CALNICA pipeline (Hsiao et al. 2010). For data taken with ACS WFC in the z_{850} filter, we incorporate an SED-dependent AC (see the Appendix).

Following the procedures outlined in Kowalski et al. (2008) and Amanullah et al. (2010), we add our SNe Ia to the Union2 compilation. Of the 20 SNe Ia of our SNe, 14 pass the Union2 selection cuts, ten of which are at $z > 1$. The strategy of targeting high-redshift galaxy clusters results in a factor-of-two improvement in the yield per *HST* orbit of well-measured SNe Ia beyond $z = 1$ and a factor-of-three to -five improvement for SNe hosted by early-type galaxies. For WFC3, with its smaller field of view, the advantage of a cluster search is even greater.

We use the new Union2.1 sample to constrain the properties of dark energy. SNe Ia alone constrain the existence of dark energy to very high significance. After adding constraints from the CMB, BAO, and H_0 measurements, we provide the tightest limits yet on the evolution of dark energy with time: $w_a = 0.14^{+0.60}_{-0.76}$. Our sample improves the constraints on binned ρ by 18% (including systematics) in the difficult-to-measure high-redshift bin, $1.0 < z < 1.6$. Even with a time-varying w_0–w_a model, the universe is constrained to be flat with an accuracy of 2% in Ω_k.

The results from this new cluster-hosted SN sample point the way to the next steps that are now possible with the WFC3 on *HST*, an instrument that can obtain high signal-to-noise ratio, multifilter SN Ia light curves at $z > 1$. The cluster approach, used in this paper, would make it feasible to build a significantly larger sample at these highest redshifts, evenly balanced between early- and late-type hosts. With such a sample, we can mitigate the effects of dust and evolution that may ultimately limit constraints on time-varying w.

Financial support for this work was provided by NASA through program GO-10496 from the Space Telescope Science Institute, which is operated by AURA, Inc., under NASA contract NAS 5-26555. This work was also supported in part by the Director, Office of Science, Office of High Energy and Nuclear Physics, of the U.S. Department of Energy under contract No. AC02-05CH11231, as well as a JSPS core-to-core program "International Research Network for Dark Energy" and by JSPS research grant 20040003. Support for M.B. was provided by the W. M. Keck Foundation. The work of S.A.S. was performed under the auspices of the U.S. Department of Energy by Lawrence Livermore National Laboratory in part under Contract W-7405-Eng-48 and in part under contract DE-AC52-07NA27344. The work of P.E., J.R., and D.S. was carried out at the Jet Propulsion Laboratory, California Institute of Technology, under a contract with NASA. T.M. and Y.I. have been financially supported by the Japan Society for the Promotion of Science through its Research Fellowship. H.H. acknowledges support from a VIDI grant from the Netherlands Organization for Scientific Research (NWO) and a Marie Curie International Reintegration Grant. N.S., C.L., and S.P. wish to thank the support and hospitality of the Aspen Center for Physics, where much of this paper was written. We thank Jay Anderson, L. E. Bergeron, Ralph Bohlin, Roelof de Jong, Anton Koekemoer, Jennifer Mack, Bahram Mobasher, Adam Riess, Kenneth Sembach, and ACS and NICMOS teams at the Space Telescope Science Institute for their advice on the *HST* data calibration. We also thank Alex Conley for calibration discussions. Finally, we thank our referee, who carefully read our paper and gave valuable feedback.

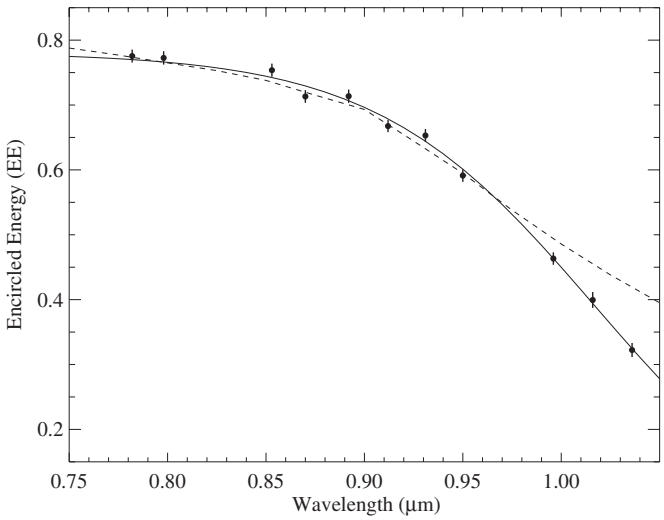

Figure 10. Wavelength vs. encircled energy (EE) fraction for a 3 pixel aperture. The solid line is a fit (Equation (A1)) to the measured data points. The dotted line is the relation from Sirianni et al. (2005).

APPENDIX

ACS COLOR-DEPENDENT APERTURE CORRECTION

The scattering of long-wavelength photons (>8000 Å) within the ACS CCDs causes the PSF of images taken in the ACS z_{850} band to depend on the SED of the source (Sirianni et al. 2005; Jee et al. 2007). The SED-dependent PSF means that ACs also depend on the SED (Riess et al. 2007). In this section, we describe how we derive ACs for our observations taken with the ACS z_{850} band.

We use two stars (GRW70 and GD72 from ACS programs PID9020 and PID10720; Riess et al. 2007) to measure the AC as a function of wavelength. The stars were observed with 15 narrowband filters between 7660 Å and 10360 Å. We processed the data in the same way as the SN Ia images. To derive the AC, we compare the flux in two apertures, one with a 3 pixel radius and the other with a 110 pixel radius (the radius used for defining the zero point). Errors from removing the sky are the dominant source of the uncertainty of this measurement.

The measured encircled energy (EE) and its best-fit curve for a 3 pixel radius are shown as a function of wavelength in Figure 10. We apply an AC to the observed flux with this best-fit curve. Figure 11 demonstrates that the i_{775}–z_{850} color is not accurate enough for SNe Ia to infer an accurate AC. Therefore, we need to introduce an SED-weighted AC.

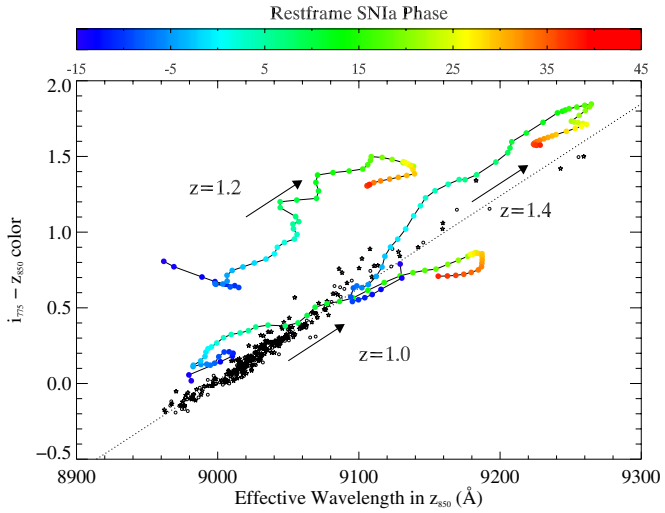

Figure 11. Wavelength vs. $i_{775} - z_{850}$ color: solid asterisks are stars from the Gunn–Stryker catalog (Gunn & Stryker 1983); open asterisks are stars from the Pickles catalog (Pickles 1998). The dotted line is the best-fit line to the stellar locus. SN Ia loci (Hsiao et al. 2007) are plot for three redshifts with color-coded phases and arrows which show the direction of the phase evolution. The SN Ia loci deviate from the stellar locus as the SED is different. Therefore, $i_{775} - z_{850}$ colors are not accurate enough to perform aperture corrections, necessitating the introduction of an SED-weighted aperture correction.

(A color version of this figure is available in the online journal.)

We find that the best-fit EE curve can be described with

$$\mathrm{EE}(\lambda) = \frac{1}{1.28 + 1.45 \times 10^{-8} \times \exp(17.99 \times \lambda)}, \quad \text{(A1)}$$

where λ is wavelength in μm. The formula is valid in wavelength for virtually all the F850LP filter.

Since the SED of an SN Ia is a function of redshift and phase, so is the AC (Riess et al. 2007). We demonstrate two methods to account for this dependence. The first method, "Method I," calculates the AC iteratively using the SED produced by SALT2. The advantage of this method is that the final aperture-corrected fluxes can be used with the standard throughputs and zero points. The second method, "Method II," computes a new zero point and F850LP throughput for direct use with the flux measurements that have not been aperture-corrected. We note here that an apparent color difference between SNe with only ACS data and those that also had NICMOS observations was seen unblinded *before* the development of these methods, so the relative colors of the ACS-only and NICMOS-included subsamples should not be considered blinded.

Both methods give the same answer, although the error in the color from "Method II" is slightly larger than that of "Method I," because the effective wavelength of the z_{850} shifts toward the i_{775} filter, thus shortening the wavelength separation of the two filters. For this paper, we adopt "Method II" and report all results using this method.

A.1. Method I: Iterative Approach

The magnitude of an object in the Vega magnitude system is defined (Fukugita et al. 1995; Sirianni et al. 2005) as

$$m = -2.5 \log_{10} \left(\frac{\int \lambda R f_\lambda d\lambda}{\int \lambda R f_{\lambda\,\mathrm{Vega}} d\lambda} \right), \quad \text{(A2)}$$

where λ is wavelength, R is the system response, f_λ is the SED of the object (e.g., SN Ia), and $f_{\lambda\,\mathrm{Vega}}$ is the SED of Vega. We define the Vega magnitude zero point (Zpt) as

$$\mathrm{Zpt}_{\mathrm{Vega}} = 2.5 \log_{10} \left(\int \lambda R f_{\lambda\,\mathrm{Vega}} d\lambda \right). \quad \text{(A3)}$$

Equation (A2) can then be rewritten as

$$m = -2.5 \log_{10} \left(\int \lambda R f_\lambda d\lambda \right) + \mathrm{Zpt}_{\mathrm{Vega}}. \quad \text{(A4)}$$

The observed magnitude, m_{obs}, within a given aperture is

$$m_{\mathrm{obs}} = -2.5 \log_{10} \left(\int \lambda\, R\, \mathrm{EE}(\lambda)\, f_\lambda d\lambda \right) + \mathrm{Zpt}_{\mathrm{Vega}}, \quad \text{(A5)}$$

where EE(λ) is the wavelength-dependent EE, which can be derived from Equation (A1).

We define the SED-dependent AC (Δm_{corr}) as

$$\Delta m_{\mathrm{corr}} = -2.5 \log_{10} \left(\frac{\int \lambda\, R\, \mathrm{EE}(\lambda)\, f_\lambda d\lambda}{\int \lambda R f_\lambda d\lambda} \right). \quad \text{(A6)}$$

In practice, we do not know f_λ in advance, so we cannot compute the AC directly. Instead, we derive it iteratively using the SED derived from fitting the SN Ia light curve with SALT2 as input to the next iteration. With this method, we use the STScI filter response function and zero points.

A.2. Method II: Modified Filter with Zero Point

We can rewrite Equation (A5) as

$$m_{\mathrm{obs}} = -2.5 \log_{10} \left(\frac{\int \lambda\, R\, \mathrm{EE}(\lambda) f_\lambda d\lambda}{\int \lambda\, R\, \mathrm{EE}(\lambda)\, f_{\lambda\,\mathrm{Vega}} d\lambda} \right) + \mathrm{Zpt}_{\mathrm{Vega}} - 2.5 \log_{10} \left(\int \lambda\, R\, \mathrm{EE}(\lambda)\, f_{\lambda\,\mathrm{Vega}} d\lambda \right). \quad \text{(A7)}$$

Effectively, the last term serves as a zero-point offset for a given aperture radius.

We rewrite Equation (A7) as

$$m_{\mathrm{obs}} = -2.5 \log_{10} \left(\frac{\int \lambda\, R\, \mathrm{EE}(\lambda)\, f_\lambda d\lambda}{\int \lambda\, R\, \mathrm{EE}(\lambda)\, f_{\lambda\,\mathrm{Vega}} d\lambda} \right) + \mathrm{Zpt}_{\mathrm{Vega}} - \Delta\mathrm{Zpt}_{\mathrm{Vega}}; \quad \text{(A8)}$$

$\Delta\mathrm{Zpt}_{\mathrm{Vega}} = 0.438$ for a 3 pixel radius aperture and the z_{850} filter. We interpret Equation (A8) as a magnitude measurement that uses a modified filter response, $R\,\mathrm{EE}(\lambda)$, and an adjusted zero point, $\mathrm{Zpt}_{\mathrm{Vega}} - \Delta\mathrm{Zpt}_{\mathrm{Vega}}$. We then run SALT2 using the counts in a fixed aperture, the modified filter response, and the adjusted zero point.

REFERENCES

Albrecht, A., Bernstein, G., Cahn, R., et al. 2006, arXiv:astro-ph/0609591
Aldering, G., Adam, G., Antilogus, P., et al. 2002, Proc. SPIE, 4836, 61
Amanullah, R., Lidman, C., Rubin, D., et al. 2010, ApJ, 716, 712
Amanullah, R., Stanishev, V., Goobar, A., et al. 2008, A&A, 486, 375
Barker, E. A., Laidler, V. G., & Koekemoer, A. M. 2007, Removing Post-SAA Persistence in NICMOS Data (Instrument Science Report. NICMOS ISR 2007-001; Baltimore: Space Telescope, Science Institute), http://www.stsci.edu/hst/nicmos/documents/isrs/isr_2007_001.pdf
Astier, P., Guy, J., Regnault, N., et al. 2006, A&A, 447, 31
Barbary, K., Aldering, G., Amanullah, R., et al. 2012a, ApJ, 745, 31 (Paper II)
Barbary, K., Aldering, G., Amanullah, R., et al. 2012b, ApJ, 745, 32 (Paper VI)
Barbary, K., Dawson, K. S., Tokita, K., et al. 2009, ApJ, 690, 1358

Beckwith, S. V. W., Stiavelli, M., Koekemoer, A. M., et al. 2006, AJ, 132, 1729
Blakeslee, J. P., Franx, M., Postman, M., et al. 2003, ApJ, 596, L143
Bohlin, R. C. 2007, Photometric Calibration of the ACS CCD Cameras (Instrument Science Report. ACS ISR 2007-06; Baltimore: Space Telescope Science Institute), http://www.stsci.edu/hst/acs/documents/isrs/isr0706.pdf
Bohlin, R. C., Lindler, D. J., & Riess, A. G. 2005, Grism Sensitivities and Apparent Non-Linearity (Instrument Science Report. NICMOS ISR 2005-002; Baltimore: Space Telescope Science Institute), http://www.stsci.edu/hst/nicmos/documents/isrs/isr_2005_002.pdf
Bohlin, R. C., Lindler, D. J., & Riess, A. G. 2006, NICMOS Count Rate Dependent Non-Linearity in G096 and G141 (Instrument Science Report. NICMOS ISR 2006-002; Baltimore: Space Telescope Science Insitute), http://www.stsci.edu/hst/nicmos/documents/isrs/isr_2006_002.pdf
Bohringer, H., Mullis, C., Rosati, P., et al. 2005, The Messenger, 120, 33
Bouwens, R. J., Illingworth, G. D., Blakeslee, J. P., & Franx, M. 2006, ApJ, 653, 53
Brodwin, M., Stern, D., Vikhlinin, A., et al. 2011, ApJ, 732, 33
Bruzual, G., & Charlot, S. 2003, MNRAS, 344, 1000
Bundy, K., Ellis, R. S., & Conselice, C. J. 2005, ApJ, 625, 621
Conley, A., Howell, D. A., Howes, A., et al. 2006, AJ, 132, 1707
Contreras, C., Hamuy, M., Phillips, M. M., et al. 2010, AJ, 139, 519
Copeland, E. J., Sami, M., & Tsujikawa, S. 2006, Int. J. Mod. Phys. D, 15, 1753
Dahlen, T., McLaughlin, H., Laidler, V., et al. 2008, Improvements to Calnica (Instrument Science Report. NICMOS ISR 2008-002; Baltimore: Space Telescope Science Insitute), http://www.stsci.edu/hst/nicmos/documents/isrs/isr_2008_002.pdf
Dawson, K. S., Aldering, G., Amanullah, R., et al. 2009, AJ, 138, 1271
de Jong, R. S., Bergeron, E., Riess, A., & Bohlin, R. 2006, NICMOS Count-Rate Dependent Nonlinearity Tests Using Flatfield Lamps (Instrument Science Report. NICMOS ISR 2006-001; Baltimore: Space Telescope Science Insitute), http://www.stsci.edu/hst/nicmos/documents/isrs/isr_2006_001.pdf
Dickinson, M., Giavalisco, M., & GOODS Team. 2003, in The Mass of Galaxies at Low and High Redshift, ed. R. Bender & A. Renzini (Berlin: Springer-Verlag), 324
Doi, M., Tanaka, M., Fukugita, M., et al. 2010, AJ, 139, 1628
Duffy, A. R., Schaye, J., Kay, S. T., & Dalla Vecchia, C. 2008, MNRAS, 390, L64
Dunkley, J., Komatsu, E., Nolta, M. R., et al. 2009, ApJS, 180, 306
Eisenhardt, P. R. M., Brodwin, M., Gonzalez, A. H., et al. 2008, ApJ, 684, 905
Eisenstein, D. J., Zehavi, I., Hogg, D. W., et al. 2005, ApJ, 633, 560
Fadeyev, V., Aldering, G., & Perlmutter, S. 2006, PASP, 118, 907
Fruchter, A. S., & Hook, R. N. 2002, PASP, 114, 144
Fukugita, M., Ichikawa, T., Gunn, J. E., et al. 1996, AJ, 111, 1748
Fukugita, M., Shimasaku, K., & Ichikawa, T. 1995, PASP, 107, 945
Garnavich, P. M., Jha, S., Challis, P., et al. 1998, ApJ, 509, 74
Gilbank, D. G., Gladders, M. D., Yee, H. K. C., & Hsieh, B. C. 2011, AJ, 141, 94
Gladders, M. D., & Yee, H. K. C. 2005, ApJS, 157, 1
Gunn, J. E., & Stryker, L. L. 1983, ApJS, 52, 121
Guth, A. H. 1981, Phys. Rev. D, 23, 347
Guy, J., Astier, P., Baumont, S., et al. 2007, A&A, 466, 11
Guy, J., Astier, P., Nobili, S., Regnault, N., & Pain, R. 2005, A&A, 443, 781
Guy, J., Sullivan, M., Conley, A., et al. 2010, A&A, 523, A7
Hamuy, M., Phillips, M. M., Suntzeff, N. B., et al. 1996, AJ, 112, 2391
Hamuy, M., Trager, S. C., Pinto, P. A., et al. 2000, AJ, 120, 1479
Heyer, I., Richardson, M., Whitmore, B., & Lubin, L. 2004, The Accuracy of WFPC2 Photometric Zeropoints (Instrument Science Report. WFPC2 ISR 2004-001; Baltimore: Space Telescope Science Insitute), http://www.stsci.edu/instruments/wfpc2/wfpc2_isr/wfpc2_isr0401.pdf
Hicken, M., Challis, P., Jha, S., et al. 2009a, ApJ, 700, 331
Hicken, M., Wood-Vasey, W. M., Blondin, S., et al. 2009b, ApJ, 700, 1097
Hilton, M., Collins, C. A., Stanford, S. A., et al. 2007, ApJ, 670, 1000
Hilton, M., Stanford, S. A., Stott, J. P., et al. 2009, ApJ, 697, 436
Holtzman, J. A., Marriner, J., Kessler, R., et al. 2008, AJ, 136, 2306
Hsiao, E. Y., Conley, A., Howell, D. A., et al. 2007, ApJ, 663, 1187
Hsiao, E. Y., Suzuki, N., Ripoche, P., et al. 2010, 2010 Space Telescope Science Institution Calibration Workshop, ed. Deustua & Oliveira (Baltimore: Space Telescope Science Institute), http://www.stsci.edu/~INS/2010CalWorkshop/hsiao.pdf
Huang, X., Morokuma, T., Fakhouri, H. K., et al. 2009, ApJ, 707, L12
Jee, M. J., Blakeslee, J. P., Sirianni, M., et al. 2007, PASP, 119, 1403
Jee, M. J., Dawson, K. S., Hoekstra, H., et al. 2011, ApJ, 737, 59
Jee, M. J., Rosati, P., Ford, H. C., et al. 2009, ApJ, 704, 672
Kaiser, M. E., Kruk, J. W., McCandliss, S. R., et al. 2010, arXiv:1001.3925
Kelly, P. L., Hicken, M., Burke, D. L., Mandel, K. S., & Kirshner, R. P. 2010, ApJ, 715, 743
Kessler, R., Becker, A. C., Cinabro, D., et al. 2009, ApJS, 185, 32
Knop, R. A., Aldering, G., Amanullah, R., et al. 2003, ApJ, 598, 102
Koekemoer, A. M., Fruchter, A. S., Hook, R. N., & Hack, W. 2002, in The 2002 HST Calibration Workshop: Hubble after the Installation of the ACS and the NICMOS Cooling System, ed. S. Arribas, A. Koekemoer, & B. Whitmore (Baltimore, MD: Space Telescope Science Institute), 337
Komatsu, E., Smith, K. M., Dunkley, J., et al. 2011, ApJS, 192, 18
Kowalski, M., Rubin, D., Aldering, G., et al. 2008, ApJ, 686, 749
Kuznetsova, N., Barbary, K., Connolly, B., et al. 2008, ApJ, 673, 981
Lampeitl, H., Smith, M., Nichol, R. C., et al. 2010, ApJ, 722, 566
Liddle, A. R., & Lyth, D. H. 2000, Cosmological Inflation and Large-Scale Structure (Cambridge: Cambridge Univ. Press)
Linder, E. V. 2003, Phys. Rev. Lett., 90, 091301
Mannucci, F., Della Valle, M., Panagia, N., et al. 2005, A&A, 433, 807
Maraston, C. 2005, MNRAS, 362, 799
McGraw, J. T., Zimmer, P. C., Ackermann, M. R., et al. 2010, Proc. SPIE, 7739, 773929
Mei, S., Blakeslee, J. P., Stanford, S. A., et al. 2006, ApJ, 639, 81
Melbourne, J., Dawson, K. S., Koo, D. C., et al. 2007, AJ, 133, 2709
Melbourne, J., Wright, S. A., Barczys, M., et al. 2005, ApJ, 625, L27
Ménard, B., Kilbinger, M., & Scranton, R. 2010, MNRAS, 406, 1815
Meyers, J., et al. 2012, ApJ, submitted
Miknaitis, G., Pignata, G., Rest, A., et al. 2007, ApJ, 666, 674
Mobasher, B., & Riess, A. 2005, A Test of Possible NICMOS Non-linearity (Instrument Science Report. NICMOS ISR 2005-003; Baltimore: Space Telescope Science Insitute), http://www.stsci.edu/hst/nicmos/documents/isrs/isr_2005_003.pdf
Morokuma, T., Tokita, K., Lidman, C., et al. 2010, PASJ, 62, 19
Navarro, J. F., Frenk, C. S., & White, S. D. M. 1997, ApJ, 490, 493
Norgaard-Nielsen, H. U., Hansen, L., Jorgensen, H. E., Aragon Salamanca, A., & Ellis, R. S. 1989, Nature, 339, 523
Peng, C. Y., Ho, L. C., Impey, C. D., & Rix, H. 2002, AJ, 124, 266
Percival, W. J., Reid, B. A., Eisenstein, D. J., et al. 2010, MNRAS, 401, 2148
Perlmutter, S., Aldering, G., della Valle, M., et al. 1998, Nature, 391, 51
Perlmutter, S., Aldering, G., Goldhaber, G., et al. 1999, ApJ, 517, 565
Perlmutter, S., Marvin, H. J., Muller, R. A., et al. 1991, in Supernovae, ed. S. E. Woosley (New York: Springer-Verlag), 727
Pickles, A. J. 1998, PASP, 110, 863
Postman, M., Franx, M., Cross, N. J. G., et al. 2005, ApJ, 623, 721
Postman, M., Lubin, L. M., Gunn, J. E., et al. 1996, AJ, 111, 615
Regnault, N., Conley, A., Guy, J., et al. 2009, A&A, 506, 999
Riess, A., & Bergeron, E. 2008, Bright Earth Persistence in NICMOS (Instrument Science Report. NICMOS ISR 2008-001; Baltimore: Space Telescope Science Institute), http://www.stsci.edu/hst/nicmos/documents/isrs/isr_2008_001.pdf
Riess, A. G., Filippenko, A. V., Challis, P., et al. 1998, AJ, 116, 1009
Riess, A. G., Kirshner, R. P., Schmidt, B. P., et al. 1999, AJ, 117, 707
Riess, A., & Mack, J. 2004, Time Dependence of ACS WFC CTE Corrections for Photometry and Future Predictions (Instrument Science Report. ACS ISR 2004-006; Baltimore: Space Telescope, Science Institute), http://www.stsci.edu/hst/acs/documents/isrs/isr0406.pdf
Riess, A. G., Macri, L., Casertano, S., et al. 2011, ApJ, 730, 119
Riess, A. G., Strolger, L.-G., Casertano, S., et al. 2007, ApJ, 659, 98
Riess, A. G., Strolger, L.-G., Tonry, J., et al. 2004, ApJ, 607, 665
Ripoche, P., et al. 2012, ApJ, submitted
Rosati, P., Stanford, S. A., Eisenhardt, P. R., et al. 1999, AJ, 118, 76
Rosati, P., Tozzi, P., Gobat, R., et al. 2009, A&A, 508, 583
Sahlén, M., Viana, P. T. P., Liddle, A. R., et al. 2009, MNRAS, 397, 577
Sand, D. J., Graham, M. L., Bildfell, C., et al. 2011, ApJ, 729, 142
Santos, J. S., Rosati, P., Gobat, R., et al. 2009, A&A, 501, 49
Schlegel, D. J., Finkbeiner, D. P., & Davis, M. 1998, ApJ, 500, 525
Schmidt, B. P., Suntzeff, N. B., Phillips, M. M., et al. 1998, ApJ, 507, 46
Sirianni, M., Clampin, M., Hartig, G. F., et al. 1998, Proc. SPIE, 3355, 608
Sirianni, M., Jee, M. J., Benítez, N., et al. 2005, PASP, 117, 1049
Smith, J. A., Tucker, D. L., Kent, S., et al. 2002, AJ, 123, 2121
Spergel, D. N., Verde, L., Peiris, H. V., et al. 2003, ApJS, 148, 175
Strazzullo, V., Rosati, P., Pannella, M., et al. 2010, A&A, 524, 17
Stubbs, C. W., High, F. W., George, M. R., et al. 2007, PASP, 119, 1163
Sullivan, M., Conley, A., Howell, D. A., et al. 2010, MNRAS, 406, 782
Sullivan, M., Ellis, R. S., Aldering, G., et al. 2003, MNRAS, 340, 1057
Sullivan, M., Le Borgne, D., Pritchet, C. J., et al. 2006, ApJ, 648, 868
Tremonti, C. A., Heckman, T. M., Kauffmann, G., et al. 2004, ApJ, 613, 898
Wood-Vasey, W. M., Miknaitis, G., Stubbs, C. W., et al. 2007, ApJ, 666, 694
Zimmer, P. C., McGraw, J. T., Ackermann, M. R., et al. 2010, Proc. SPIE, 7735, 77358D